An Investigation of Coupled Atmospheric and Oceanic Boundary Layers Using Large-Eddy Simulation

PETER P. SULLIVAN,[a] JAMES C. MCWILLIAMS,[b] AND EDWARD G. PATTON[a]

[a] NSF National Center for Atmospheric Research, Boulder, Colorado
[b] Department of Atmospheric and Oceanic Sciences, University of California, Los Angeles, Los Angeles, California

(Manuscript received 5 July 2024, in final form 11 November 2024, accepted 18 January 2025)

ABSTRACT: The marine atmospheric boundary layer (ABL) and oceanic boundary layer (OBL) are a two-way coupled system. At the ocean surface, the ABL and OBL share surface fluxes of momentum and buoyancy that incorporate variations in sea surface temperature (SST) and currents. To investigate the interactions, a coupled ABL–OBL large-eddy simulation (LES) code is developed and exercised over a range of atmospheric stability. At each time step, the coupling algorithm passes oceanic currents and SST to the atmospheric LES, which in turn computes surface momentum, temperature, and humidity fluxes driving the oceanic LES. Equations for each medium are time advanced using the same time step but utilize different grid resolutions: the horizontal grid resolution in the ocean is approximately four times finer, e.g., $(\Delta x_o, \Delta x_a) = (1.22, 4.88)$ m. Interpolation and anterpolation (its adjoint) routines connect the atmosphere and ocean surface layers. In the simplest setup of a statistically horizontally homogeneous flow, the largest scale ABL turbulent shear-convective rolls leave an imprint on the OBL currents in the upper layers. This result is shown by comparing simulations that use coupling rules that are applied either instantaneously at every x–y grid point or averaged across an x–y plane. The spanwise scale of the ABL turbulence is ~1000 m, while the depth of the OBL is ~20 m. In these homogeneous, fully coupled cases, the large-scale spatially intermittent turbulent structures in the ABL modulate SST, currents, and the connecting momentum and buoyancy fluxes, but the mean profiles in each medium are only slightly different.

KEYWORDS: Atmosphere-ocean interaction; Boundary layer; Surface layer; Surface fluxes

1. Introduction

The marine atmospheric boundary layer (ABL) and oceanic boundary layer (OBL) are a coupled system with two-way feedbacks with unknown dependencies on the horizontal heterogeneity of the oceanic surface. The coupling in the oceanic submesoscale regime $0.1 < L_x < 10$ km and smaller is an active research topic as discussed in recent reviews (McWilliams 2016, 2021; Taylor and Thompson 2023). The submesoscale regime features density fronts, filaments, and vortices (i.e., eddies) with lifetimes of hours to days, and "submesoscale turbulence" is readily observed in sun glitter (e.g., Munk et al. 2000) and in ocean simulations utilizing nested grids (e.g., Gula et al. 2014; Renault et al. 2019). The submesoscale oceanic dynamics experiment (S-MODE), conducted off the Northern California coast, is a recent attempt to utilize new observational systems to examine the interaction of submesoscale turbulence and the lower atmosphere (Farrar et al. 2020; Wineteer et al. 2024). Investigations of submesoscale turbulence have also fostered renewed interest in ABL–OBL coupling in nominally "horizontally homogeneous" oceanic surfaces, i.e., in the absence of submesoscale oceanic features and in particular ask the question under what conditions can atmospheric turbulence leave an imprint on the upper ocean or vice versa. Our emphasis is the coupling of shear-convective turbulence in the ABL with the OBL as found in large-eddy simulation (LES). This is a natural first question before moving into the heterogeneous submesoscale coupling regimes (e.g., Sullivan et al. 2020, 2021; Sullivan and McWilliams 2022).

To provide background for our study, we briefly review important characteristics of the stratified ABL and OBL that motivate our study of a coupled ABL–OBL system. Over land, the ABL coherent structures vary from convective plumes to turbulent "shear-convective rolls" (SCRs), to hairpin vortices, and to stably stratified temperature fronts (Sullivan et al. 2016) depending on the stability parameter $-h/L$, where h is the ABL depth and L is the surface layer Monin–Obukhov stability parameter:

$$L = -\frac{u_*^3}{\beta \kappa Q_{v,*}}. \tag{1}$$

The term u_* is the friction velocity, $\beta = g/\theta_o$ is the buoyancy parameter with g gravity and θ_o is the still air potential temperature, $\kappa = 0.4$ is the von Kármán constant, and $Q_{v,*}$ is the virtual potential temperature flux.

In the free convection limit $-h/L \rightarrow \infty$ (Schmidt and Schumann 1989), the length and velocity scales of the canonical ABL are (h, w_*), where the Deardorff (1970) convective velocity scale is $w_*^3 = \beta h Q_{v,*}$. In the shear-driven limit $-h/L \rightarrow 0$ with zero surface temperature flux $Q_{v,*} = 0$, the relevant scales become (h, u_*) (Moeng and Sullivan 1994). There have been numerous studies of the so-called weakly convective shear ABL between these two limits. The studies over land use LES (e.g., Deardorff 1972; Moeng and Sullivan 1994; Conzemius and Fedorovich 2006; Salesky et al. 2017; Jayaraman and Brasseur 2021) and observations (e.g., LeMone 1973; Kristovich 1993; Weckwerth et al. 1997; Chen et al. 2001;

Corresponding author: Peter P. Sullivan, pps@ucar.edu

DOI: 10.1175/JAS-D-24-0149.1

Alcayaga et al. 2022)—for reviews, see Weckwerth et al. (1997) and Salesky et al. (2017). Over a wide range of $-h/L$ in the weakly convective shear regime, buoyancy dominates and the relevant velocity scale is primarily w_*. In the weakly convective shear regime, the dominant turbulent structures are narrow in width streaks near the surface that merge upward in the ABL into elongated shear-convective rolls or shear-convective turbulence. In the middle and upper ABL, the primary axis of SCR is aligned with the mean wind direction with a much narrower y spacing (Moeng and Sullivan 1994; Salesky et al. 2017). SCRs are ABL depth filling structures with a streamwise extent that approaches the mesoscale (Alcayaga et al. 2022). A sudden transition in the coherence of the shear-convective rolls appears to occur near $-h/L \approx 0.43$ (Jayaraman and Brasseur 2021). Over the ocean, the near-surface longitudinal length scale of surface streaks is observed to be very long, e.g., $\mathcal{O}(100)$ km in gale force winds (see Fig. 1 Chen et al. 2001). At large values of $-h/L > 10$, the SCRs merge into closed cells, supporting convective plumes; compared to the SCR, the convective plumes propagate slowly in the horizontal directions. The SCRs are important as they are long lived in the ABL and then can couple with the OBL.

The nighttime unstable OBL in a weakly convective shear regime is usually viewed as a shear-driven layer with the effect of surface waves modeled primarily using a surface roughness z_o. The parameterization of oceanic surface fluxes can include a host of wave boundary layer effects, e.g., spray, bubbles, wave breaking, surface currents, misaligned wind and wave fields, thermal cool skin, radiation, diurnal warm layers, and remotely generated swell (e.g., see Fairall et al. 1996, 2003; Edson et al. 2007; Hanley et al. 2010; Sullivan and McWilliams 2018; Wong and Minnett 2018; Richter et al. 2019; Cronin et al. 2019; Mazella et al. 2024). Many of these near surface effects are subgrid-scale in LES, and most are not considered here. Surface waves are, however, particularly important to OBL mixing under both unstable and stable forcing as they generate Langmuir cells; this effect is modeled using the asymptotic theory of fast waves on slow currents first developed by Leibovich (1983). The OBL mixed regime of shear, buoyancy, and surface waves is referred to as Langmuir turbulence (LT) and is a frequent topic of LES and observational studies (e.g., McWilliams et al. 1997; Harcourt and D'Asaro 2008; Sullivan and McWilliams 2010; Kukulka et al. 2010; Belcher et al. 2012; Hamlington et al. 2014; D'Asaro et al. 2014; Sullivan and McWilliams 2019, 2024). The oceanic thermal (cool) skin layer with thickness a fraction of a millimeter determines the sea surface temperature (SST) and interfacial heat fluxes but cannot be resolved by practical LES grids.

To examine the ABL–OBL in horizontally homogeneous conditions and the role of coherent structures in the interaction dynamics, we utilize a newly developed coupled LES code that simulates both marine boundary layers simultaneously using the same time step but with different grid resolutions. Recently, Brilouet et al. (2021, 2024) considered a case study of the evolution of diurnal warm layers in the DYNAMO field campaign (Moum et al. 2014) using a partially coupled ABL–OBL model; their model uses LES in the ABL coupled to a single column 1D oceanic mixed layer model. Also, our coupled ABL–OBL differs from free-surface simulations where the overlying atmosphere is neglected (e.g., Shen and Yue 2001), ABL simulations with a moving wave field (e.g., Sullivan et al. 2014), coupled air–water simulations carried out in small domains using direct numerical simulations (e.g., Fulgosi et al. 2003), coupling schemes that only utilize single column 1D boundary layer models (e.g., Harris et al. 1996), and mesoscale simulations that couple 1D boundary layer models in large horizontal domains (e.g., Perlin et al. 2014).

The outline of the manuscript is as follows. The coupled LES is briefly described in section 2, section 3 describes the LES experiments, the results are discussed in section 4, and section 5 provides the conclusions from the work.

2. Large-eddy simulation

The dynamics of the atmospheric and oceanic boundary layers are assumed to be described by a conventional LES model for a high-Reynolds number Boussinesq flow with system rotation, for example, see Moeng (1984), McWilliams et al. (1997), Sullivan et al. (2007), and Sullivan and Patton (2011) for ABL and OBL descriptions of the code. The LES model includes transport equations for the following: momentum $\rho\mathbf{u}$, with ρ being the fluid density and $\mathbf{u}$ being the velocity vector, temperature θ, specific humidity q, and subgrid-scale (SGS) energy e. The divergence-free (incompressible) condition determines the elliptic pressure variable $\pi = p/\rho$. The wind and current vectors $\mathbf{u} \equiv u_i = (u, v, w)$ are aligned with the Cartesian coordinates $\mathbf{x} \equiv x_i = (x, y, z)$; these directions are also referred to as (streamwise, spanwise vertical) directions in the narrative. The rotation vector is $\mathbf{f} = (0, 0, f)$, with f being the Coriolis parameter. Buoyancy in the vertical velocity equation is defined in terms of temperature assuming a linear equation of state $b = \beta(\theta_v - \theta_o)$, where β is the buoyancy parameter chosen for air or seawater. The virtual potential temperature in the ABL (e.g., Wyngaard 2010, p. 183),

$$\theta_v = \theta(1 + 0.61q), \tag{2}$$

is used in the ABL buoyancy term, where θ is the potential temperature in units of kelvins and q is the specific humidity ratio, i.e., the mass of water vapor to the total mass of air. In the ABL, the buoyancy term in the SGS energy equation (Moeng and Sullivan 2015) is parameterized following Deardorff (1980) and Heus et al. (2010).

Virtual potential temperature θ_v is used in the atmospheric Monin–Obukhov (MO) surface layer routine that evaluates surface fluxes dependent on the stability parameter z/L. The MO iteration begins assuming a saturated sea surface $q = q_{\mathrm{sat}}$ (e.g., Stull 1988, p. 276) and along with SST extrapolated from the OBL interior computes surface θ_v ($z = 0$) from (2). The iteration with oceanic currents u_o, v_o extrapolated from the first OBL model level, along with horizontal winds and temperature at the first ABL model level u, v, θ, generates surface momentum fluxes τ_{uw}, τ_{vw} in the x, y directions, sensible temperature flux Q_*, and latent humidity flux q_* using bulk formulas. The OBL surface momentum and heat fluxes are matched to the ABL values:

TABLE 1. Atmosphere and ocean properties used in the simulations.

Symbol	Variable	Atmosphere	Ocean	Units
ρ	Density	1	1000	kg m^{-3}
C_p	Specific heat	1004	4200	J kg^{-1} K^{-1}
β	Buoyancy parameter	3.27×10^{-2}	1.96×10^{-3}	m s^{-2} K^{-1}
f	Coriolis parameter	10^{-4}	10^{-4}	s^{-1}
L_e	Latent heat of vaporization	2.5×10^6		J kg^{-1}
p_*	Reference pressure	100×10^3		N m^{-2}

$$\rho\tau_{uw}|_o = \rho\tau_{uw}|_a, \tag{3a}$$

$$\rho\tau_{vw}|_o = \rho\tau_{vw}|_a, \tag{3b}$$

$$\rho C_p Q_*|_o = \rho C_p Q_*|_a + \rho L_e q_*|_a, \tag{3c}$$

where $|_o$ and $|_a$ denote the ocean and atmosphere, respectively. In (3), ρ, C_p, and L_e are the density and specific heat in the ABL and OBL and latent heat of vaporization in the ABL, respectively. The ABL and OBL friction velocities are defined from $u_*|_a = \sqrt{|\tau_a|/\rho_a}$ and $u_*|_o = \sqrt{|\tau_o|/\rho_o}$, where the vector magnitude in the ABL or OBL is $|\tau| = \tau_{uw}^2 + \tau_{vw}^2$. The OBL temperature flux is $Q_*|_o$, and the ABL surface virtual potential temperature flux $Q_{v,*} = Q_* + 0.61\theta q_*$. The fluxes computed from (3) are spectrally interpolated in x–y across the water surface, and then, the LES equations in the ABL and OBL are separately integrated forward in time using the same time step. The use of Monin–Obukhov similarity to compute the surface fluxes is described in section 3.

At the present time, the air–water interface is flat, i.e., there are no resolved surface waves in the simulations. The ABL LES model adopts θ, q as conserved variables and assumes unsaturated conditions (no clouds). The OBL LES model includes phase-averaged wave–current interactions as described in Leibovich (1983), McWilliams et al. (1997), and Sullivan et al. (2007, 2012). These are incompressible Boussinesq equations that use the original vortex force formulation with the vortex force $\mathbf{u}_s \times \boldsymbol{\omega}$ contributing to all three resolved momentum equations, where $\mathbf{u}_s$ is the Stokes drift vector and $\boldsymbol{\omega}$ is the resolved vorticity. Suzuki and Fox-Kemper (2016) describe alternative but equivalent forms of the wave-averaged equations. Details of the Stokes drift computation are given in section 3.

Only a single equation for potential temperature in the OBL is included, $\theta_v \equiv \theta$, and salt is not considered; Nurser and Griffies (2019) describe the details for specifying salt fluxes. In the OBL, SST is a key component in our ABL–OBL coupling and we simply adjust the OBL SST using the cool skin parameterization that depends on bulk wind speed proposed by Wong and Minnett (2018); their empirical correlation reduces the skin temperature compared to the 5-m temperature using the expression $\Delta\theta_{\text{skin–5m}} = 0.2$–$0.24\exp(-U_{10}/3.6)$, where U_{10} is the mean wind speed at the reference height $z = 10$ m. The different physical constants used in the ABL and OBL are given in Table 1.

The same numerical algorithm is used in the ABL and OBL. The horizontal differencing is pseudospectral and second-order finite differencing in the vertical direction. A compact third-order Runge–Kutta scheme is used for the time advancement, and the time step is chosen to satisfy a Courant–Fredrich–Lewys (CFL) condition based on the maximum velocity relative to the spatial discretization; the time step Δt is typically chosen by the atmospheric conditions because of the relatively fast winds compared to the slow currents. The vertical grid is positive upward with the grid origin, $z = 0$, located at the water surface.

The code parallelization is based on the 2D domain decomposition described in Sullivan and Patton (2011) that uses custom built matrix transposes to carry out fast Fourier transforms and the tridiagonal solution of the pressure Poisson equation. At runtime, the total number of processors requested is split unequally between the atmospheric and oceanic LES, and more processors are used in the oceanic simulation to accommodate the denser grid and finer horizontal grid spacing Δx_o spanning the much larger horizontal extent of the atmospheric grid L_x (see section 3). Typically, the ratio of oceanic to atmospheric processors is between 2:1 and 4:1 but is easily adjusted and is accomplished using the message passing interface (MPI) routine MPI_COMM_SPLIT; the latter routine is used to split the world communicator at run time. Ideally, for the same Δt, the computational work in the ABL with fewer processors is equal to or less than the work in the OBL with more processors.

Only two new routines are added to the LES code: a routine that averages (or anterpolates) the finer-scale oceanic surface currents and SST to the coarser horizontal atmospheric grid, and a second routine that spectrally interpolates the coarser atmospheric fluxes to the finer horizontal oceanic grid. The x–y average of the fluxes is identical on the ABL and OBL grids at every time step. The strategy of splitting the world communicator allows the coupling to use the already developed code for the oceanic and atmospheric boundary layers (e.g., Sullivan and McWilliams 2019, 2022). Essentially, two LESs are run simultaneously with MPI: one in the atmosphere and a second in the ocean. The two LESs only communicate in exchanging SST, currents, and momentum, temperature, and humidity fluxes. The use of multiple LES domains is also described in our "fringe" simulations (Sullivan et al. 2020, 2021; Sullivan and McWilliams 2022).

3. Coupled simulations

Recent observational field campaigns by Moum et al. (2014), Farrar et al. (2020), Shroyer et al. (2021), and Mahadevan et al. (2021) find a rich variety of coupled air–sea interactions occurring at varying scales. In the current paper, we are loosely guided by these observations but concentrate on canonical situations that feature nominally horizontally homogeneous ABL–OBL regimes. Our coupled simulations are posed as process studies of air–sea phenomena and in particular the coupling of atmospheric SCRs with the OBL. We target unstable ABL conditions with varying geostrophic wind speeds and surface forcing conditions that are deemed horizontally homogeneous. Under the expectation that the unstable atmospheric regime will feature SCR structures, an anisotropic computational domain is used in the LES with dimensions $(L_x, L_y, L_{z,a}) = (2.5, 5, 1.2)$ km. The wider L_y domain compared to the L_x domain is chosen to allow multiple roll patterns to exist in our computational domain (see section 4a). Shear-convective turbulent rolls are typically ABL filling structures with an elongated x axis compared to their relatively narrow spanwise y axis; i.e., they are horizontally anisotropic structures.

The discretization of the ABL–LES uses $(N_x, N_y, N_z)_a = (512, 1024, 256)$ mesh points with the first vertical grid level for w located at $z_1 = 3$ m. A nonuniform vertical grid is built using algebraic stretching with the stretching factor between vertical grid cells $K = 1.00267$. The OBL–LES domain spans the same horizontal dimensions as the ABL with a vertical domain $L_{z,o} = -60$ m. Grid mesh $(N_x, N_y, N_z)_o = (2048, 4096, 128)$ points cover the OBL with its first vertical level for w located at $z_1 = -0.4$ m using a stretching factor $K = 1.00244$ between vertical grid levels. Thus, the ratio of horizontal grid spacings in the ABL and OBL is $\Delta x_a/\Delta x_o = 4.88\ \text{m}/1.22\ \text{m} = 4$.

In the OBL, wind-wave equilibrium corresponds to wave age $c_p/U_{10} = 1.2$, where c_p is the peak wave phase speed and U_{10} is the atmospheric wind speed at the reference height $z = 10$ m. The wave slope $ak = 0.1$ is assumed for fixing an exponentially decaying Stokes drift profile $\mathbf{u}_s(z)$; the OBL is then in a wave-impacted regime as the turbulent Langmuir number $La_t \sim 0.3$ over the geostrophic wind speed range considered here (McWilliams et al. 1997; Harcourt and D'Asaro 2008; Belcher et al. 2012). An x–y average Stokes drift profile is applied in the OBL at every time step.

The simulations vary the geostrophic wind speed $U_g = [5–15]\ \text{m s}^{-1}$ along with an initial prescribed SST jump $\delta\theta_i$ between the ABL and OBL; the same initial mean (temperature, humidity) profiles $[\theta(z), q(z)]$ are used in all simulations, and for a particular simulation, U_g is constant and aligned with the x axis. In addition, a free convection simulation with $U_g = 0$ and a weakly stably stratified ABL with $U_g = 8\ \text{m s}^{-1}$ in a smaller domain are also performed for comparison (see section 4f). To generate unstable ABLs, the initial ABL–OBL temperature jump is set $\delta\theta_i = 1$ or 3 K. To account for the oceanic cool skin, the SST is further reduced using the correlation proposed by Wong and Minnett (2018). Of course, as the simulation progresses and the turbulence develops the unstable jump $\delta\theta$ between the ABL and OBL is automatically reduced depending on the coupling, the ABL warms and the OBL cools. The initial temperature and humidity profiles in the ABL are composed of two segments (see Fig. 4)

$$\theta(z) = \begin{cases} \theta_i & : 0 < z < h_i \\ \theta_i + (z - h_i)0.01\ \text{K m}^{-1} & : h_i < z < L_{z,a} \end{cases}, \tag{4}$$

$$q(z) = \begin{cases} 0.010\ \text{kg kg}^{-1} & : 0 < z < h_i \\ 0.010\ \text{kg kg}^{-1} - (z - h_i)10^{-5}\ \text{m}^{-1} & : h_i < z < L_{z,a} \end{cases}, \tag{5}$$

where the initial ABL height $h_i = 250$ m and $L_{z,a} = 1100$ m is the ABL–LES domain height. The initial temperature value is $\theta_i = 298$ or 296 K. The surface saturation specific humidity $q_{\text{sat}} \approx 0.622 e_{\text{sat}}/p_* \sim 0.0214\ \text{kg kg}^{-1}$, where e_{sat} is the saturation vapor pressure (e.g., Stull 1988, p. 276). The initial humidity profile is chosen to roughly match that used in the case study of Brilouet et al. (2021, Fig. 2) but in a shallower ABL. The initial temperature in the ocean is simply (accounting for negative z values)

$$\theta(z) = \begin{cases} \theta_i & : 0 > z > -h_i \\ \theta_i + (z + h_i)\ 0.021\ \text{Km}^{-1} & : -h_i > z > L_{z,o} \end{cases}, \tag{6}$$

where the initial mixed layer depth $h_i = 13.3$ m and the initial oceanic temperature $\theta_i = 299$ K. Thus, the ABL–OBL initial temperature jump is an unstable jump $\delta\theta_i = (1, 3)$ K. The initial horizontal wind in the ABL is set equal to the geostrophic value, while the initial currents in the ocean are set equal to zero.

The ABL surface fluxes are computed from the Monin–Obukhov similarity relationships using temperature, humidity, and wind speed at the first model level in the ABL grid assuming a roughness length $z_o = 2 \times 10^{-4}$ m given by Large and Pond (1981). Identical roughness for momentum and temperature is used at every horizontal grid point in the ABL–LES. Two variations on the surface coupling rules between the ABL and OBL are used. The first method applies the surface conditions instantaneously at every x–y grid point; i.e., the surface fluxes, SST, and currents are applied horizontally "point-by-point." In the second method, the surface conditions are imposed by applying "x–y" averaging, i.e., the ABL surface fluxes, and the OBL SST and currents are first averaged in a horizontal plane, and these averages are used in the coupling. The x–y averaging rule removes the turbulence spatial variability between the ABL and OBL, in particular the large-scale SCR.

The use of local instantaneous surface exchange coefficients between the ABL and OBL adopted here is an approximation partly supported by the analysis of surface flux conservation laws described by Wyngaard et al. (1998). At the small time and space scales used in the present work, these conservation equations are stochastic, but their coupling with the LES equations yields only marginal improvements in the prediction of the nondimensional mean shear and mean temperature gradient profiles over a rough stationary surface. Wyngaard et al. (1998) concluded the form of the LES subgrid-scale model has a much greater impact on the overall LES predictive capabilities than the surface flux exchange rule. More work is needed to clarify the time and space dependencies of the ABL–OBL surface exchange rules.

TABLE 2. Bulk properties in the simulations: (left) ABL and (right) OBL columns.

	ABL										OBL			
Run	U_g (m s^{-1})	$\delta\theta_i$ (K)	u_* (m s^{-1})	w_* (m s^{-1})	$Q_{v,*}$ (K m s^{-1})	F_h (W m^{-2})	F_q (W m^{-2})	h (m)	$-L$ (m)	$-h/L$	u_* (m s^{-1})	w_* (m s^{-1})	Q_* (K m s^{-1})	h (m)
$U15$	15	1	0.382	0.698	0.019	−1.6	285	542	223	2.43	0.0121	0.016	6.75×10^{-5}	28.3
$U15_a$	15	1	0.383	0.699	0.019	−1.6	284	541	223	2.43	0.0121	0.016	6.74×10^{-5}	28.3
$U10$	10	1	0.279	0.651	0.018	1.4	229	464	91.7	5.1	0.0088	0.013	5.4×10^{-5}	22.6
$U10_a$	10	1	0.279	0.651	0.018	1.3	229	467	91.6	5.1	0.0088	0.013	5.5×10^{-5}	22.6
$U10C$	10	3	0.292	0.857	0.035	16.0	263	545	54.3	10.0	0.0092	0.014	6.66×10^{-5}	23.1
$U10C_a$	10	3	0.291	0.854	0.035	16.0	261	541	53.5	10.1	0.0092	0.044	6.60×10^{-5}	23.1
$U5$	5	1	0.160	0.554	0.012	1.7	148	415	25.0	16.6	0.0050	0.011	3.6×10^{-6}	19.8
$U5_a$	5	1	0.159	0.554	0.012	1.7	147	415	24.8	16.7	0.0050	0.011	3.6×10^{-6}	19.8
UF	0	1	0.002	0.303	0.0023	0.3	26.7	373	4.1×10^{-4}	$>10^5$	7.29×10^{-5}	0.061	6.5×10^{-6}	17.4
US	8	−1	0.175		−0.0060	−3.7	−33.6	138	−65.7	−2.1	0.0055		-8.85×10^{-6}	19.7

A list of the simulations along with bulk statistics is provided in Table 2. The statistics include friction velocity u_*, surface buoyancy flux $Q_{v,*}$, sensible heat flux $F_h = \rho C_p Q_*$, latent heat flux $F_q = \rho L_e q_*$, ABL and OBL boundary layer depth h, Monin–Obukhov length L, atmospheric stability parameter $-h/L$, and Deardorff convective velocity scale $w_* = (\beta Q_{v,*} h)^{1/3}$. The simulation run names that use x–y average surface coupling are indicated by a subscript $()_a$, e.g., $U10_a$ is the simulation with $U_g = 10$ m s^{-1} that uses x–y average surface coupling conditions. In Table 2, the ABL and OBL friction velocity and virtual potential temperature flux vary because of the differences in ρ and C_p. For the unstable simulations, the range of the stability parameter $-h/L = [2.4–10^5]$, i.e., the range is from weak to strongly unstable conditions.

Given the above choices of grid mesh, the computational work in the ABL using 512 processors is less than 30% of the work in the OBL using 2048 processors. A simulation with $U_g = 10$ m s^{-1} and an integration over 60 000 time steps, with $\Delta t \sim 0.28$ s, takes about 90 wall clock hours.

4. Results

Statistics are computed by averaging in the x–y directions and in time, indicated by angle brackets $\langle\rangle$. For cases with $U_g = 15$ m s^{-1}, the time averaging interval is $t = [2.8–4.6]$ h; for cases with $U_g = 10$ m s^{-1}, the time averaging interval is $t = [2.1–4.8]$ h; for cases with $U_g = 5$ m s^{-1}, the time interval is $t = [2.8–5.7]$ h; and for the free-convection case, the time interval $t = [13.9–16.6]$ h. The vortex force in the OBL induces a rapid transition to a turbulent state, and the OBL transition roughly keeps pace with the ABL turbulence evolution. Inspection of the time history of bulk statistics, e.g., (u_*, Q_*, h) in the ABL and OBL, shows that the coupled system is in a quasi-steady state over the chosen time interval, and thus, the above averaging windows are considered adequate. To obtain a fair comparison, the same time averaging window is used for simulations with the same U_g but with different surface coupling rules. Variables are decomposed into a mean $\langle\rangle$ and turbulent fluctuation $()'$, i.e., a variable $f = \langle f \rangle + f'$. Total turbulent fluxes that include both the resolved and SGS contributions are indicated by $()_{\text{tot}}$.

a. Flow visualization in the ABL and OBL

A wide spectrum of scales, ranging from meters to kilometers, is captured by the coupled LES as shown in Fig. 1 from case $U10$, taken at a late time in the simulations $t = 4.73$ h. This example, truncated in the y–z plane, shows a large downdraft in the ABL, generated by one branch of an SCR, impinging on the oceanic surface, while Langmuir turbulence generates its own smaller scale downdraft–updraft pairs in the OBL. SCRs are long lived but spatially and temporally variable structures. Their axis is roughly aligned with the mean wind

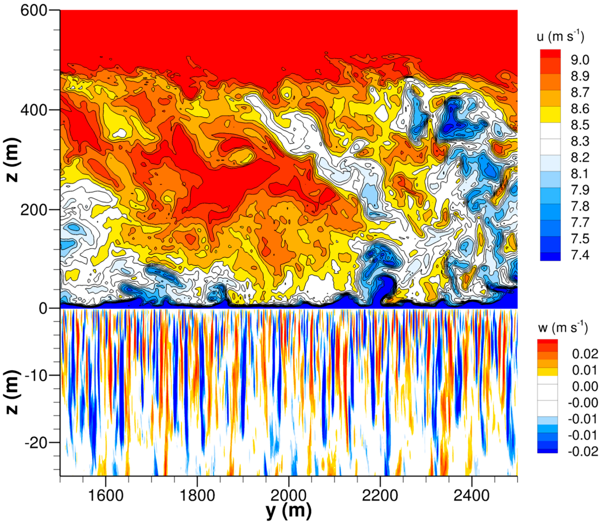

FIG. 1. Snapshot of LES results in a y–z plane from the coupled ABL–OBL simulation $U10$ driven by geostrophic winds $U_g = 10$ m s^{-1} and virtual potential surface buoyancy flux $Q_{v,*} = 0.018$ K m s^{-1}. (top) Streamwise velocity u in the ABL over $z = [0, 600]$ m, and (bottom) simultaneously, vertical velocity w in the OBL over $z = [-25, 0]$ m. For clarity, only a fraction of the 5-km y domain is shown; the z axis in the OBL is expanded compared to the ABL. Notice the coherent structures in the flow: a large downdraft in the ABL centered over the region $y = [1600–2200]$ m, a signature of ABL shear-convective turbulence, and the small-scale updraft–downdraft pattern characteristic of LT in the OBL. There is a hint of internal wave generation below the thermocline.

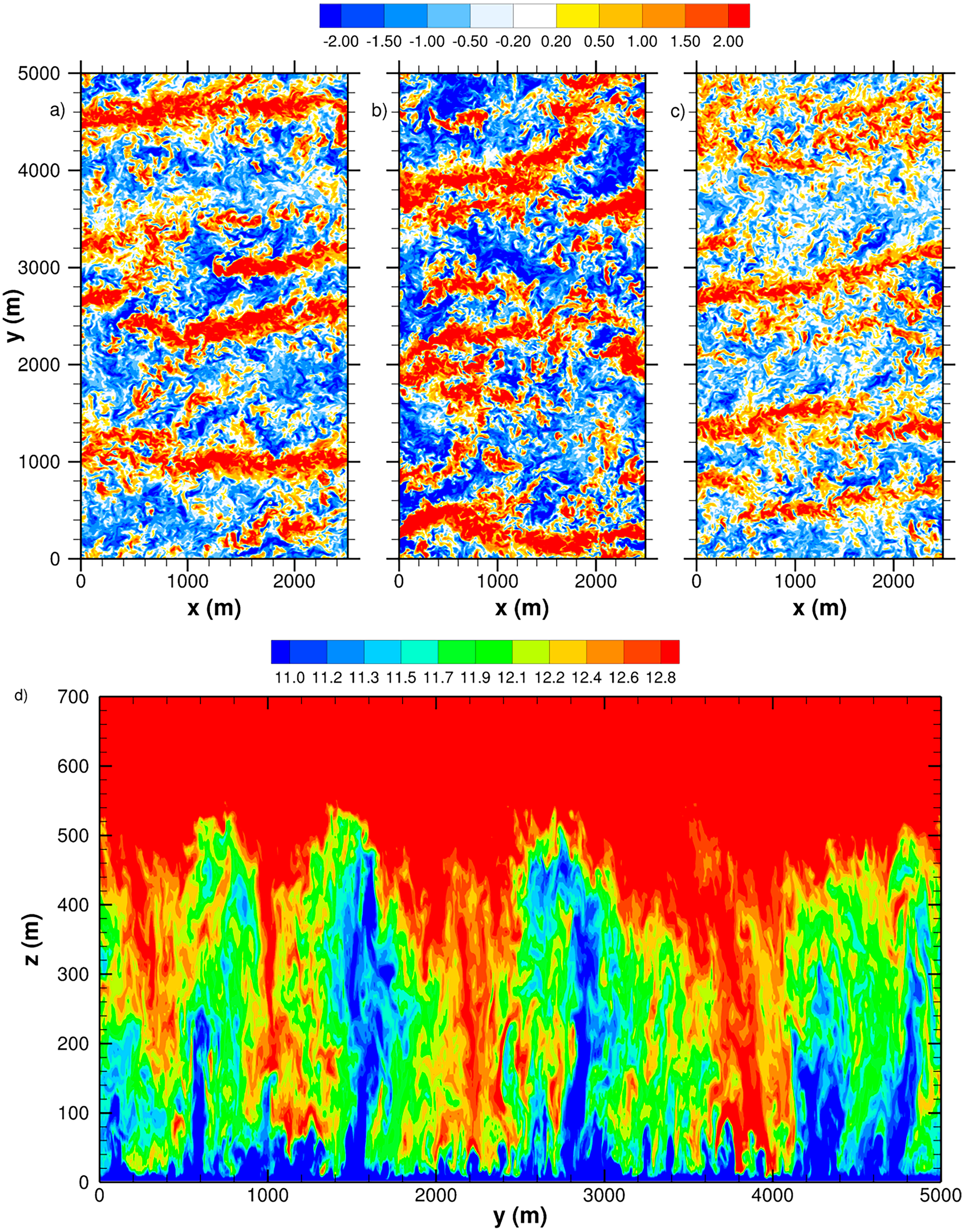

FIG. 2. (a)–(c) Snapshot of vertical velocity w showing typical ABL turbulence SCRs from simulations with geostrophic winds $U_g = (10, 10, 15)$ m s^{-1}, run names ($U10$, $U10C$, $U15$). The x–y plane is in the lower boundary layer at $z = 160$ m. The color bar is in nondimensional units w/u_*. (d) Snapshot of total u field showing typical ABL shear-convective turbulence in a y–z plane at $x = 1250$ m from simulation $U15$. The color bar is in units of meters per second (m s^{-1}).

direction with a spanwise distribution and magnitude that depends on the ABL stability $-h/L$. An example of the structures in our coupled simulations is given in Fig. 2, which shows the distribution of vertical velocity w in x–y planes from simulations ($U10$, $U10C$, $U15$) with geostrophic winds $U_g = (10, 10, 15)$ m s^{-1}; these x–y slices are in the lower ABL $z = 160$ m or $z/h = (0.344, 0.239, 0.295)$, respectively, and are taken at a late time in the simulations. The simulations ($U10$, $U10C$) are driven by the same geostrophic wind but with the initial temperature between the ABL and OBL $\delta\theta_i = (1, 3)$, respectively; the latter temperature jump increases the buoyancy forcing by almost a factor of two, which

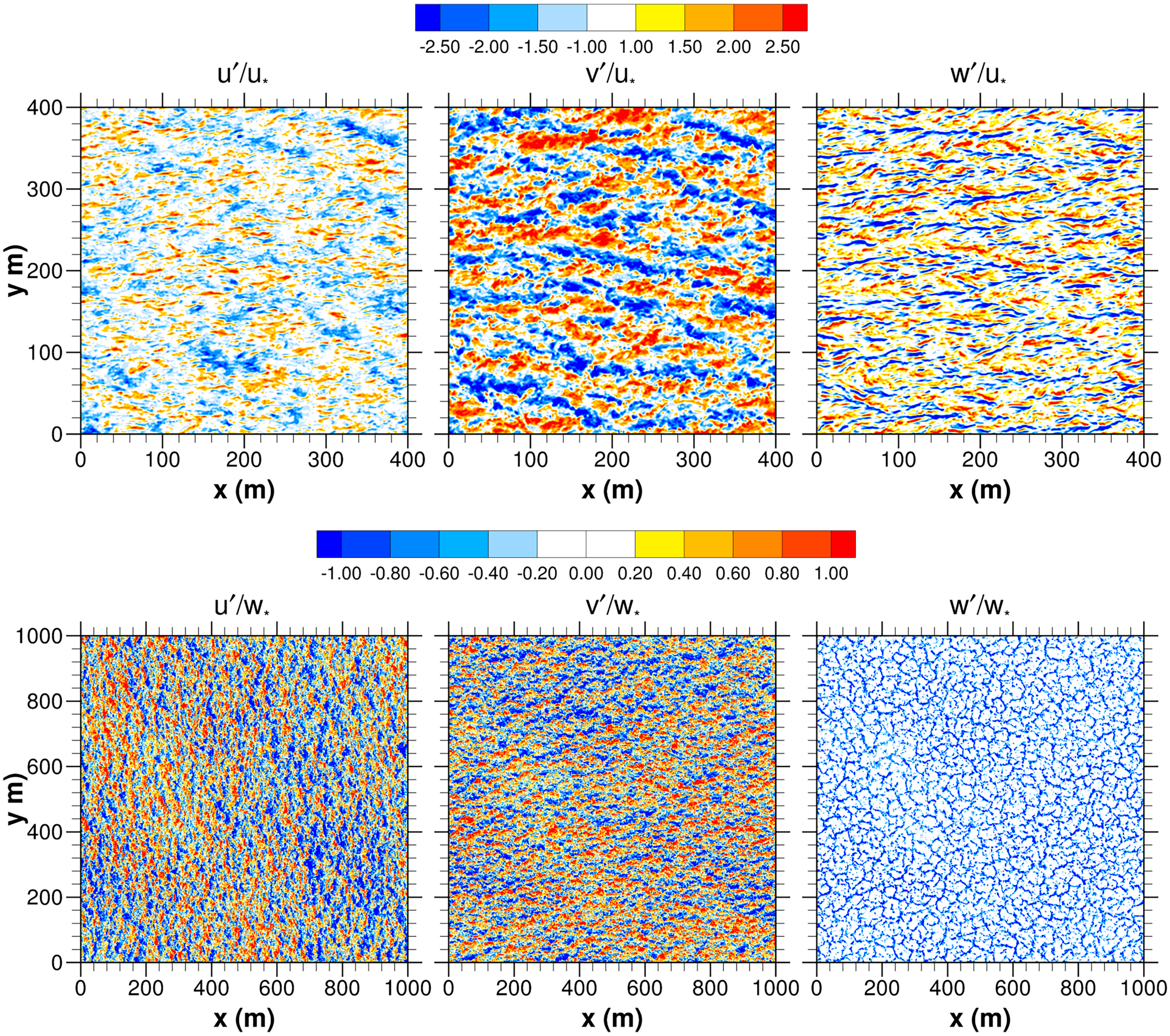

FIG. 3. (top left),(top middle) OBL horizontal fluctuating velocities $(u', v')/u_*$ at $z = -2.6$ m or $(z/h = -0.092)$ and (top right) OBL vertical velocity w'/u_* at $z = -2.8$ m $(z/h = -0.01)$ from simulation $U15$ with $U_g = 15$ m s^{-1}. The elongated streaks in the w velocity are a consequence of Langmuir cells. At the same time, the dark (blue, red) colors in the top middle panel show that LT has increased the spanwise velocity v' compared to the streamwise velocity u' shown in the left panel. (bottom left),(bottom middle) The $(u', v')/w_*$ at $z = -0.2$ m or $(z/h = -0.012)$ and (bottom right) w'/w_* at $z = -2.8$ m or $(z/h = -0.16)$ from the free convection simulation UF. The vertical velocity shows the hexagonal surface pattern of free convection; the same color bar is used for the three velocity components normalized by (u_*, w_*) for the (top, bottom) rows. The visualization of w' in the bottom row only shows downwelling, $w' < 0$. Only a fraction of the total x and y ranges are shown.

impacts the strength of the ABL–OBL coupling (Table 2). Very near the surface $z < 10$ m, the w pattern consists of thin y lines, which smoothly merge with increasing z to create the pattern in Fig. 2. In the lower ABL, Fig. 2 shows the updrafts (red colors) are narrower (in y) and stronger than the downdrafts (blue colors). Figure 2 also shows the contours of the streamwise ABL velocity u looking upwind in a y–z plane; this y–z slice is taken at $x = 1250$ m in Fig. 2c. This view shows the updrafts–downdrafts in the SCR that fill the depth of the ABL. Notice the small-scale surface eruptions in the u field and the relatively wide downdrafts from the ABL top that reach into the surface layer. The SCRs are observed to slowly translate across the spanwise direction with varying time (Sykes and Henn 1989). The visual correlation between (positive, negative) w and (negative, positive) u in Fig. 2 implies the SCRs generate a negative momentum flux $u'w' < 0$ (e.g., Moeng and Sullivan 1994). Near the surface, the SCR downdraft–updraft patterns are associated with surface splats, i.e., surface convergence-divergence zones that lead to positive and negative signed v' fluctuations.

Under typical oceanic conditions (e.g., Belcher et al. 2012), the stretching and tilting of vertical vorticity by surface waves leads to near-surface streamwise-oriented vortical rolls indicative of Langmuir turbulence (e.g., Leibovich 1983;

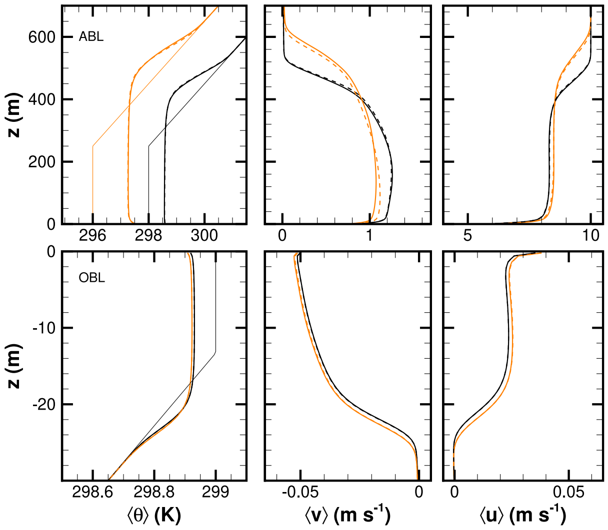

FIG. 4. ABL and OBL mean profiles of temperature and winds from simulations with $U_g = (10, 10)$ m s^{-1} run names ($U10$, $U10C$) (black, orange) lines, respectively. Temperature in the (top) ABL and (bottom) OBL. (top middle),(top right),(bottom middle),(bottom right) The $\langle v, u\rangle$ components of the wind and current. Results for simulation ($U10$, $U10C$) that include point-by-point coupling and ($U10_a$, $U10C_a$) that use x–y average coupling are indicated by solid, dashed lines. The thin line in the left panels shows the initial temperature used to start the ABL–OBL LES. The initial ABL–OBL temperature jump $\delta\theta_i = (1, 3)$ K for simulations ($U10$, $U10C$), respectively. In the bottom left panel, the thin black line is the initial OBL temperature for all simulations. Notice the ABL warms and the OBL cools to reduce the air–sea temperature difference $\delta\theta$ as time advances.

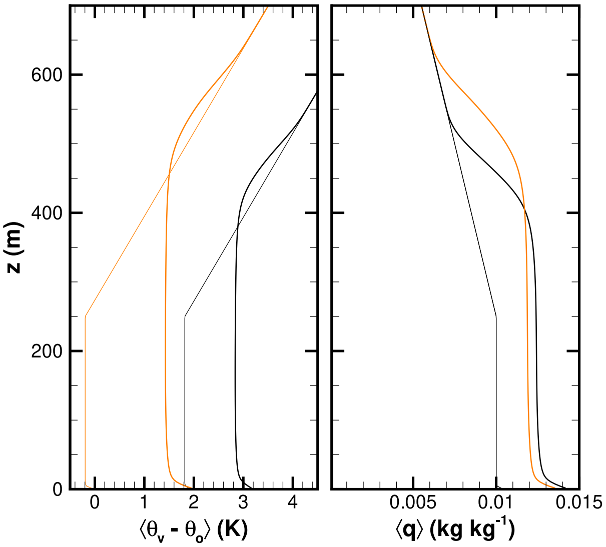

FIG. 5. ABL mean (left) virtual potential temperature $\langle\theta_v\rangle$ and (right) humidity profile $\langle q\rangle$ from simulation ($U10$, $U10C$) (black, orange) lines with $U_g = 10$ m s^{-1} at late time. The thin line in each panel shows the initial values used to start the ABL–OBL LES.

McWilliams et al. 1997; Sullivan and McWilliams 2010; Sullivan et al. 2012). The presence of LT has a significant impact on the OBL, enhancing the vertical momentum fluxes, turbulent velocity variances $\langle v'^2, w'^2\rangle$, and OBL entrainment. In leading-order wave-averaged theory, the surface waves are imposed and there is no feedback from the currents onto the wave field; see McWilliams (2022) for a more extensive discussion of coupling currents and waves. LT also efficiently mixes the OBL under stably stratified conditions (Sullivan et al. 2012; Kukulka et al. 2013). The horizontal scale of LT is at least an order of magnitude smaller than the atmospheric SCR (see section 4e). The top row of Fig. 3 is a zoom of the fluctuating oceanic flow fields $(u', v', w')/u_*$ over a (400 m)^2 patch of the oceanic surface at $z \sim -2.6$ m for $U15$. The presence of LT can readily be deduced in these images. The magnitude ordering of the LT fluctuations near the water surface is $v' > w' \gg u'$ (McWilliams et al. 1997), in contrast to flat walls where the ordering is $u' > v' \gg w'$. The image of w' shows elongated in x updraft–downdraft lines a characteristic signature of LT with large spanwise v' fluctuations near the water surface. A zoom of the ocean w' showing LT in a y–z plane is provided in Fig. 1 The bottom row of Fig. 3 is a zoom over a (1000 m)^2 ocean patch that shows the OBL velocities normalized by w_* from simulation UF. The x–y range is expanded to show a large-scale imprint of the ABL on the near-surface OBL. The bottom row right panel shows the hexagonal velocity pattern imprinted from the ABL (see section 4f). Although Stokes drift is turned on, its impact is nearly negligible as the mean winds are zero.

b. Bulk ABL and OBL profiles

Typical mean temperature and velocity profiles in the ABL and OBL are shown in Fig. 4 for simulations ($U10$, $U10_a$) and ($U10C$, $U10C_a$) with $U_g = 10$ m s^{-1}. The thin line in the temperature profiles indicates the initial condition for the LES. In ($U10$, $U10_a$), the initial jump between the atmosphere and ocean is 1 K and the atmosphere also "feels" a cool skin of approximately -0.227 K (Wong and Minnett 2018). The OBL responds to the surface buoyancy and momentum fluxes estimated from the Monin–Obukhov similarity relations applied in the ABL. The temperature jump between the ABL and OBL continually decreases as the simulation progresses and near the end of the simulation, the temperature jump $\delta\theta \sim 0.111$ K. The ABL in these simulations is only weakly convective during the analysis period; the surface sensible and latent heat fluxes are (1.4, 229) W m^{-2}, respectively. In simulation ($U10C$, $U10C_a$), the late time temperature jump is larger $\delta\theta \sim 1.18$ K, accounting for the cool skin, and the increase in buoyancy flux compared to $U10$ increases the ABL depth by ~80 m. The initial and time average values of virtual potential temperature and humidity are also shown in Fig. 5. Meanwhile, in the OBL, the average u current is well mixed below a depth of $z < -2$ m because of the combinations of Langmuir turbulence, shear forcing, and surface cooling as shown in the lower panels of Fig. 4.

The $\langle u, v\rangle$ (wind, current) are nearly unchanged by the type of surface coupling. As anticipated from the visualization, the updraft–downdraft pairs enhance the near-surface spanwise

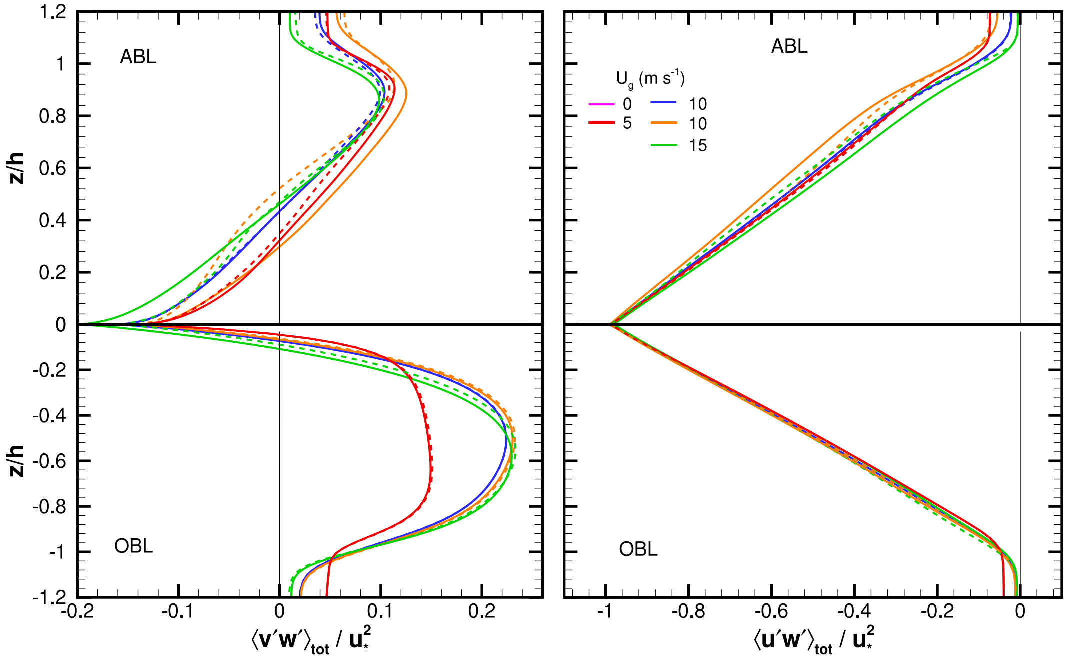

FIG. 6. Total (resolved plus SGS) spanwise and streamwise momentum flux $\langle v'w', u'w' \rangle_{\mathrm{tot}}$ in the (top) ABL and (bottom) OBL. The fluxes are (left) $\langle v'w' \rangle_{\mathrm{tot}}$ and (right) $\langle u'w' \rangle_{\mathrm{tot}}$. The fluxes are normalized by surface friction velocity u_*^2 in the ABL and OBL, and the vertical depth is normalized by the boundary layer depth h in the ABL and OBL. The solid colored lines (red, blue, orange, green) correspond to geostrophic wind $U_g = (5, 10, 10, 15)$ m s^{-1} for cases ($U5$, $U10$, $U10C$, $U15$); these simulations use point-by-point coupling conditions. The matching colored dashed lines are identical simulations but use x–y average coupling conditions.

fluctuating velocity v'. Consequently, this slightly enhances the spanwise flux $\langle v'w' \rangle_{\mathrm{tot}}$ for $U10C$ as shown in Fig. 6. While the ABL is in a weakly convective-dominated regime, the OBL is primarily driven by wind stress and waves. This is shown in Fig. 7, where vertical velocity $\langle w'^2 \rangle$ is scaled by u_* in the left panels and is scaled by w_* in the right panels. Because of LT, the OBL w variance increases by more than a factor of 2 compared to its counterpart beneath a flat wall (e.g., McWilliams et al. 1997; Harcourt and D'Asaro 2008; D'Asaro et al. 2014). In the OBL, the curves collapse using u_* scaling (left panel), whereas the ABL winds collapse using w_* scaling (right panel) as found by Deardorff (1972) over land surfaces.

Temperature fluxes in the ABL and OBL, shown in Fig. 8, are relatively unchanged by the type of surface coupling. The ABL temperature flux is dominated by its surface value with the entrainment flux a small negative fraction of the surface flux, total $\langle w'\theta'_{v,*} \rangle \sim -0.19$. However, the distribution of the OBL temperature flux is different. The entrainment flux shows an increase because of LT, larger negative values are found in the OBL compared to the surface value independent of the type of surface coupling, total $\langle w'\theta'_v \rangle / Q_{v,*} > -0.8$ for case $U15$. The ratio of the OBL depth h to the Langmuir stability length L_l, the analog of the Monin–Obukhov stability length L (Belcher et al. 2012), is $-h/L_l \ll 1$ for the simulations in Table 2. Inspection and comparison of cases ($U10$, $U10C$) in the lower panel of Fig. 8 show that the entrainment flux for $U10$ is only slightly more negative than $U10C$. In Fig. 8, the normalized surface temperature flux equals one in the ABL and OBL. The amplitude of the Stokes drift profile increases with wind speed, and thus, the OBL entrainment flux also increases (e.g., Sullivan et al. 2007, 2012). In the ABL and OBL, the normalized entrainment flux for the free-convection case, where LT is minimal in the OBL, is nearly identical $-\langle w'\theta'_v \rangle_{\mathrm{tot}} / Q_{v,*} = (0.19, 0.16)$ in the ABL and OBL, respectively.

The marine ABL is largely driven by the latent heat flux. Figure 9 depicts the profiles of the mean humidity profile $\langle q_{\mathrm{sat}} - q \rangle / \Delta q$ and humidity flux $\langle w'q' \rangle_{\mathrm{tot}} / q_*$. The humidity jump $\Delta q = \langle q_{\mathrm{sat}} - q(h) \rangle$, where $[q_{\mathrm{sat}}, q(h)]$ are the surface saturation humidity and humidity at the ABL top $z = h$, respectively. Increasing wind speed and a larger temperature jump $\delta\theta_i$ combine to increase the humidity flux profile compared to the free convection simulation. The surface latent humidity flux in Table 2 shows F_q is one to two orders of magnitude larger than F_h. Note that the mean humidity profile for ($U10$, $U10C$) is nearly identical, but the flux profile for $U10C$ is noticeably larger throughout the ABL.

c. *Filtered results*

To identify an imprint of the SCR on the upper OBL, an isotropic two-dimensional Gaussian low-pass filter with filter scale $\delta = 500$ m (e.g., Pope 2000) is applied to the fields in the ocean. Note that the filtering is expected to capture the bulk of the OBL motions as δ is much greater than the OBL depth h. The filtering is applied line-by-line first in x and then in y. The results of the filtering operation are shown in x–y planes

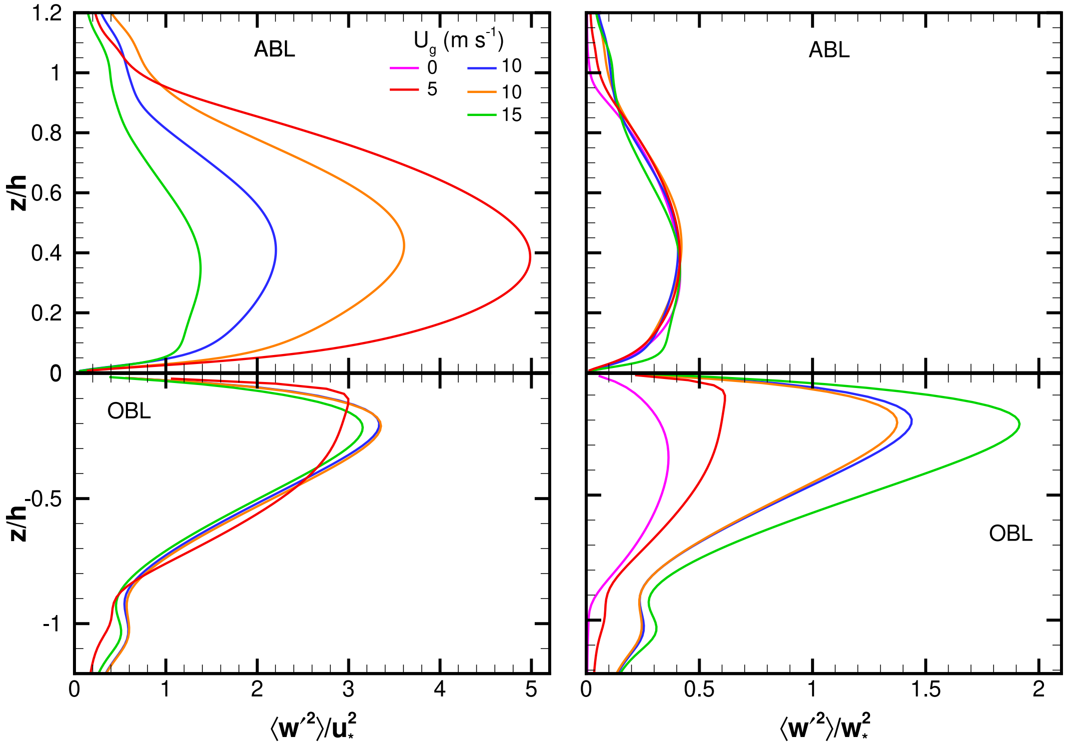

FIG. 7. Resolved w variance in the ABL and OBL for simulations with geostrophic winds $U_g = (0, 5, 10, 10, 15)$ m s^{-1}, run names (*UF*, *U*5, *U*10, *U*10*C*, *U*15), indicated by solid lines (pink, red, blue, orange, green). (left) The variances are normalized by u_*^2, and (right) the variances are normalized by w_*^2 in the atmosphere or ocean. The near-surface w variance in the OBL is increased by a factor of two by LT compared to a flat wall with no surface waves. Results for simulation *UF* are shown by pink lines in the right.

for simulations (*U*10, *U*10*C*), with $U_g = 10$ m s^{-1} in the top panels of Fig. 10. The figure shows the spatial variation in the spanwise current v'/u_* at the first level $z = -0.2$ m at a late time in the simulation; the fields are made dimensionless by the friction velocity u_* in the OBL. Examination of the top row of panels in this figure shows a clear large-scale structure oscillating in the spanwise direction for simulations (*U*5, *U*10, *U*10*C*, *U*15). The structures are intermittent in space and also time but typically span the entire x dimension of the OBL with their smaller spanwise width dependent on the atmospheric stability. For comparison, the lower row of panels in Fig. 10 show the spanwise current v'/u_*, filtered exactly as in the top row, but from simulations $(U5, U10, U10C, U15)_a$ that use x–y average coupling conditions for the SST, currents, and surface fluxes of momentum and buoyancy. Only weak randomly distributed structures are found in the OBL at a depth $z = -0.2$ m. The same color bar range is used in the top and bottom rows. Based on a qualitative interpretation of the flow visualization, simulations, *U*10, *U*10*C* produce the largest response in the ocean (see section 4e).

The SCRs in the ABL impose a large-scale wind stress on the OBL, which leads to large-scale organization of the spanwise OBL velocity v'. Figure 11 shows the fluctuating y component of the normalized wind stress τ'_{vw}/u_*^2 in the left panel and its filtered value in the right panel from simulation *U*10*C*. Note that this is the ABL wind stress (3b) interpolated to the OBL grid. The filtered field is obtained using the same Gaussian filter used to obtain the results shown in the right panel of Fig. 10c. The filtered, and also to a lesser extent the unfiltered, surface wind stress τ'_{vw} shows the same spanwise oscillation as in Fig. 10, but with a reversed sign. These large-scale surface wind stress fluctuations of course disappear in simulation $U10C_a$.

d. Correlations

To quantify the impact of the large-scale atmospheric structures on the oceanic boundary layer, we compute the normalized correlation coefficient $C_{fg}(z)$ between an atmospheric variable at a fixed height, say $f_a(z_{\text{ref}})$, and a depth-varying oceanic variable, say $g_o(z)$ (e.g., Bendat and Piersol 1971, p. 62):

$$C_{fg}(z) = \frac{\langle f_a(z_{\text{ref}})\, g_o(z) \rangle}{\sqrt{\langle f_a(z_{\text{ref}})^2 \rangle}\, \sqrt{\langle g_o(z)^2 \rangle}}, \tag{7}$$

where the angle brackets $\langle\rangle$ denote a horizontal x–y and time t average. Vertical profiles of the correlation coefficients C_{uu}, C_{vv}, C_{ww} between the atmospheric velocity $\mathbf{u}_a$ at the reference height $z_{\text{ref}} = 10$ m and the depth varying oceanic velocity $\mathbf{u}_o$ are depicted in Fig. 12. All the correlations are computed with the LES data filtered using a two-dimensional Gaussian filter with scale $\delta = 500$ m. The simulations are marked by different

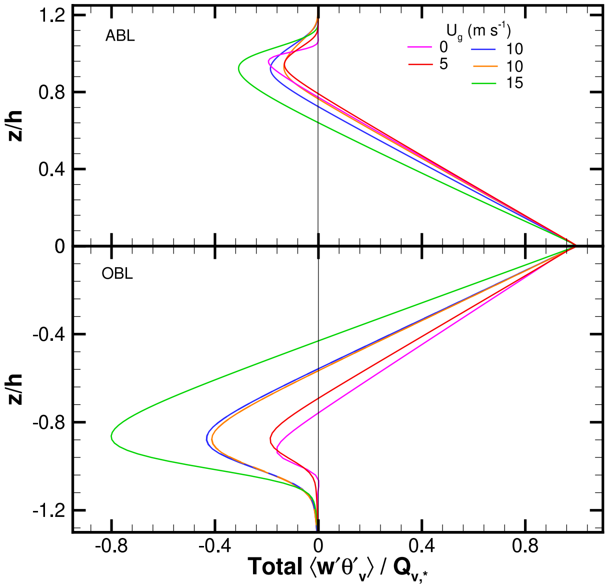

FIG. 8. Total (resolved plus SGS) virtual potential temperature flux $\langle w'\theta'_v \rangle_{\rm tot}$ normalized by surface value $Q_{v,*}$ in the (top) atmosphere and (bottom) ocean. The vertical axis is dimensionless by the ABL or OBL depth. The colored lines (pink, red, blue, orange, green) corresponding to geostrophic wind U_g = (0, 5, 10, 10, 15) m s^{-1} that use point-by-point coupling are shown as solid lines. The large entrainment flux in the OBL compared to the ABL is a consequence of LT.

colored lines for the geostrophic wind U_g = (5, 10, 15) m s^{-1}, the free-convection case is indicated by a pink line, and the stable case *US* is indicated by a dashed red line.

Inspection of the correlation coefficients for horizontal fluctuating velocities C_{uu} and C_{vv} shows a damped vertical oscillation with a penetration depth into the ocean of approximately $z_d \approx (-3, -6)$ m, respectively. Evidently, the spanwise convergence (or divergence) $\partial_y v$ in the atmospheric surface layer from the SCR leaves a modestly stronger imprint on the OBL than the streamwise fluctuating velocity, although both correlations very near the water surface are ~0.5. Compared to the other simulations, the simulation *U*10*C* with the larger ABL–OBL temperature jump shows an increased penetration depth for the C_{vv} correlation. Inspection of the vertical velocity correlation C_{ww} shows an opposite trend in the ocean compared to the horizontal velocity components, i.e., notice a negative correlation in the ocean with $w_a(z_{\rm ref}) \approx -w_o$. The surface boundary condition is $w = 0$, and at the large scales imposed by the SCR requires opposite signed downdrafts and updrafts in the atmosphere and ocean. The vertical velocity correlations go to zero at a shallow depth ~ -3 m.

The impact of stability is clearly observed in Fig. 12. The free convection simulation (no mean wind) shows the highest velocity correlations C_{uu}, $C_{vv} \sim 0.8$ near the water surface, while (C_{uu}, C_{vv}) ~0.2 or less at $z = -6$ m and $C_{ww} \sim -0.3$ at $z = -6$ m. The visualization in Fig. 13 shows a negative correlation between downdrafts–updrafts in the atmosphere and in the ocean (note the reversed color bar in the ocean). To satisfy the no-flow boundary condition $w = 0$ at $z = 0$ requires that ABL (downdrafts, updrafts) be balanced by compensating OBL (updrafts, downdrafts). Note that the structures in Fig. 13 resemble convective plumes, while the structures in Fig. 10 resemble the SCR. All the velocity correlations are zero for the simulations that use *x*–*y* averaged coupling conditions as expected based on the flow visualization in Fig. 10.

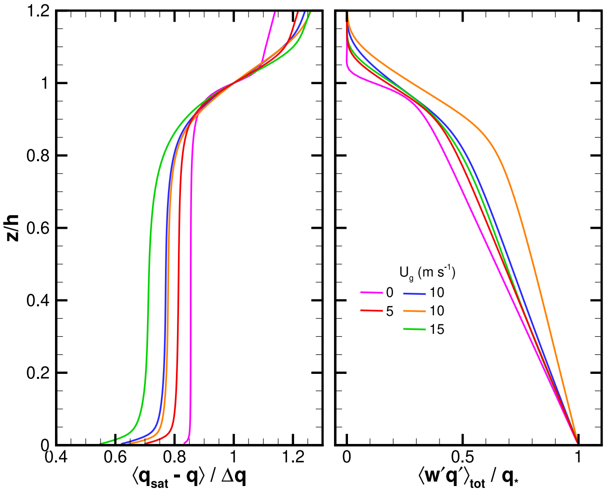

FIG. 9. (left) Humidity profile $\langle q_{\rm sat} - q \rangle / \Delta q$, where $q_{\rm sat}$ is the surface value and $\Delta q = q_{\rm sat} - q_h$. (right) Total (resolved plus SGS) humidity flux $\langle w'q' \rangle_{\rm tot}$ normalized by the surface value q_* in the ABL. The vertical axis is dimensionless by the ABL depth. The colored lines (pink, red, blue, orange, green) correspond to simulations with U_g = (0, 5, 10, 10, 15) m s^{-1} (*UF*, *U*5, *U*10, *U*10*C*, *U*15), that use point-by-point coupling.

e. Spanwise spectra

Power spectra of the spanwise velocity $E_{vv}(k_y)$ shown in Fig. 14 illustrate ABL–OBL coupling in the unstable regime. The spanwise component of the spectra is chosen to match the flow visualization of SCRs shown in Fig. 2. The upper panel of Fig. 14 shows the ABL spectra at the reference height $z_{\rm ref}$ = 10 m; notice that they are tightly grouped over the entire wavenumber range for all wind speeds, including the free convection simulation. The lower panel of Fig. 14 shows the spectral energy content in the OBL at the first level $z = -0.2$ m. There are two spectral peaks that depend on the surface coupling condition. All spectra exhibit a peak at high wavenumber $0.2 > k_y > 0.1$ m^{-1} induced by Langmuir turbulence. Because of the grid resolution, and accounting for the solution dealiasing, the highest resolved wavenumbers in the ABL and OBL are k_y = (0.428, 1.72) m^{-1}, respectively. Inspection of the spectra shows that the ABL spectrum overlaps the peak in the OBL spectrum well, suggesting that the grid resolution is adequate to capture the bulk of the ABL–OBL coupling, at least in the absence of resolved surface waves. At low wavenumber $0.001 < k_y < 0.01$, the simulations that utilize point-by-point coupling also exhibit a clear secondary peak in E_{vv} at wavenumbers k_y ~0.004 m^{-1}, i.e., at a spanwise wavelength ~1.5 km roughly matching the flow visualization in Figs. 1 and 10. The SCRs in the ABL thus leave an imprint on the OBL over a shallow depth $0 > z > -5$ m. The

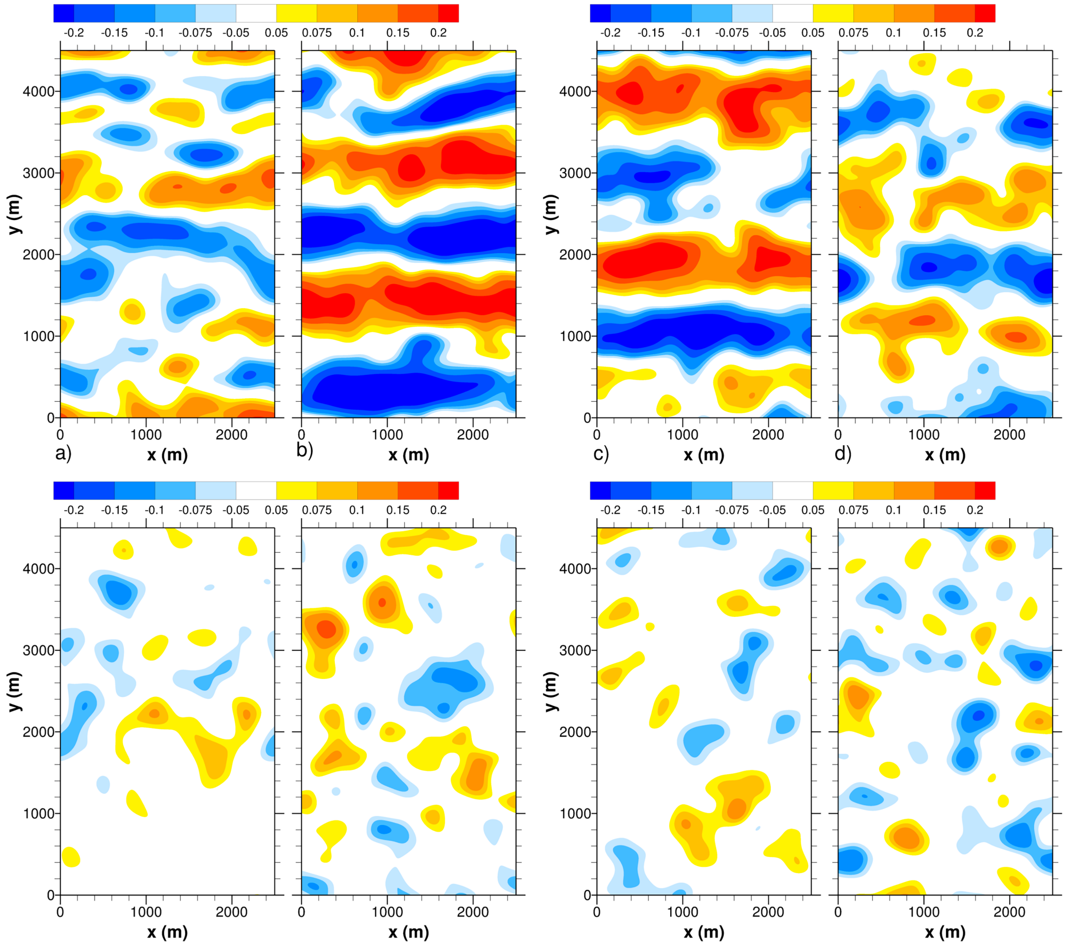

FIG. 10. Snapshot of fluctuating spanwise velocity v'/u_* in the ocean at depth $z = -0.2$ m found by filtering the OBL fields with a two-dimensional Gaussian filter of width $\delta = 500$ m. (top) Results from (a)–(d) simulations (*U*5, *U*10, *U*10*C*, *U*15) are shown from left to right. (bottom) Results from simulations $(U5, U10, U10C, U15)_a$ are shown from left to right. The simulations (*U*5, *U*10, *U*10*C*, *U*15) utilize point-by-point coupling, while the simulations $(U5, U10, U10C, U15)_a$ utilize *x*–*y* average coupling. The large-scale SCRs in the ABL create a surface splat, a convergence or divergence in the ABL fluctuating velocity v' that leaves an imprint in the v' fluctuation in the near-surface OBL in the top row.

magnitude of the spectral peak in the point-by-point coupling is 4–5 times larger than the comparable forced simulations that use *x*–*y* average coupling. This low wavenumber energy cascades to high wavenumbers in the OBL. The low wavenumber peak in the ocean spectra is a consequence of different coherent structures in the ABL, i.e., convective plumes in simulation *UF* and shear-convective rolls in simulation *U*10*C*. The results for the spanwise spectra are in agreement with the correlations shown in Fig. 12. Close inspection of the results from the highest wind simulation *U*15 provides slight evidence that the imprint of the SCR on the OBL is perhaps starting to weaken with increased wind speed as $-h/L \rightarrow 0$.

f. Free convection and stable ABLs

To explore the sensitivity to ABL stability $-h/L$, two additional coupled simulations are conducted: an ABL–OBL under free convection simulation *UF* with $-h/L > 10^5$ and a stable ABL–OBL simulation *US* with $-h/L = -2.16$ (see Table 2). The setup of the free convection simulation is identical to the simulations with wind that use point-by-point surface coupling but with $U_g = 0$. The stable case *US* is carried out in a much smaller domain with horizontal dimensions $(L_x, L_y) = (400, 400)$ m with the vertical domain in the ABL $L_{z,a} = -400$ m, and in the OBL $L_{z,o} = -60$ m. The grid mesh is 256^3 in the ABL and (768, 768, 128) in the OBL. In simulation *US*, the geostrophic wind $U_g = 8\ \mathrm{m\ s^{-1}}$ (Sullivan et al. 2016), with the initial temperature jump between the atmosphere and ocean set to $\delta\theta_i = -1$ K to produce stably stratified turbulence in the ABL.

For comparison, the results for these two cases are included in Figs. 7, 8, 12, and 14. The most striking impact of large ABL stability $-h/L > 10^5$ is shown in the correlations and spectra (Figs. 12 and 14). The *UF* case produces the largest in magnitude correlations, especially for $C_{ww} \sim -1$ at the water surface, which slowly decays with depth in the OBL, $C_{ww} \sim -0.7$ at $z = -8$ m. The spanwise spectra E_{vv} also show a significant

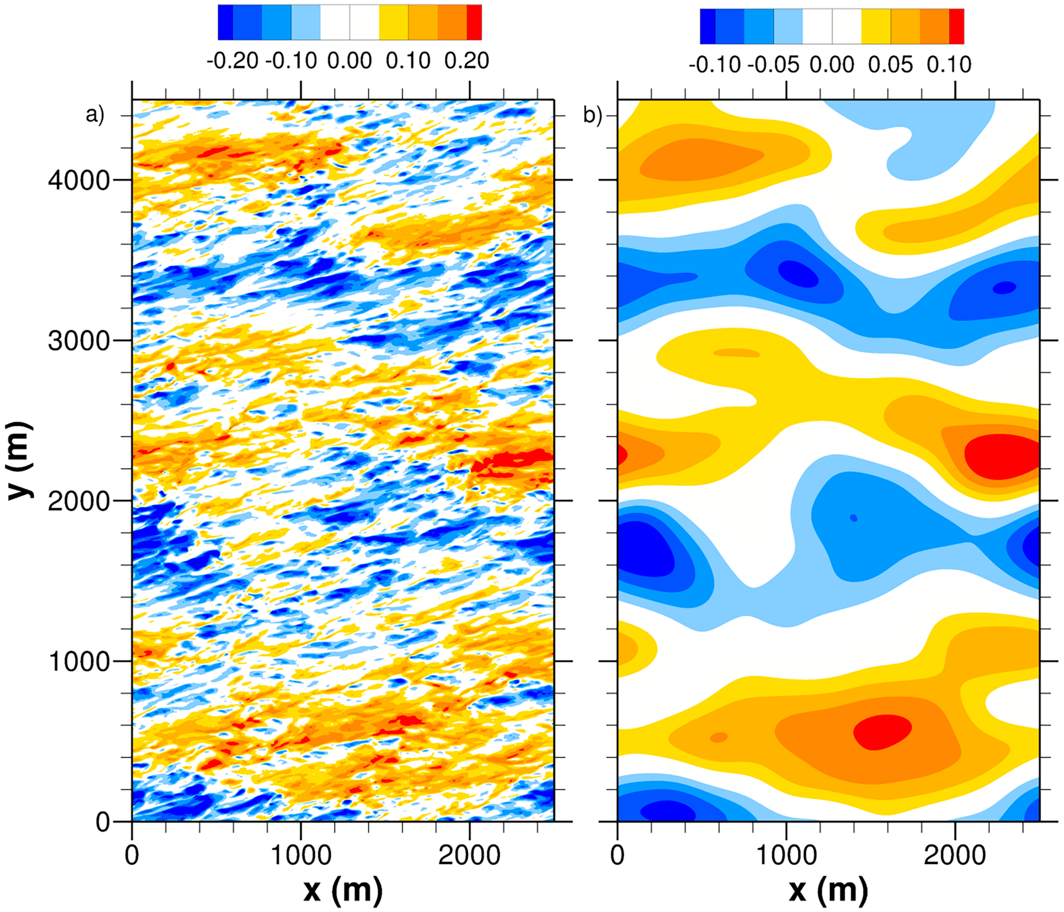

FIG. 11. (a) Fluctuating y component of momentum stress τ'_{vw} normalized by the ocean u_*^2 and (b) the filtered fluctuating momentum stress from simulation with geostrophic wind $U_g = 10$ m s^{-1}, *U10C*, at late time. The filter is a two-dimensional Gaussian filter with scale $\delta = 500$ m. The color bar is in nondimensional units of τ'_{vw}/u_*.

OBL response over all low wavenumbers $10^{-3} < k_y < 4 \times 10^{-2}$ m^{-1}, with a peak in E_{vv} near $k_y = 2.5 \times 10^{-3}$ m^{-1}. Thus, the hexagonal pattern of near-surface convection in the ABL leaves a strong imprint on the OBL as shown in Fig. 13. This figure shows a close correspondence between vertical velocity w at $z = 9$ m in the ABL and w in the OBL at $z = -1.2$ m, i.e., the largest structures in the convective ABL are also found in the OBL. This result for free convection shows that the frequency response of the ABL and OBL is well tuned when the near-surface mean advective velocity is near zero, i.e., when $U_g = 0$. The free-convection case *UF* fits our hypothesis that large-scale slow-moving structures in the ABL leave a signature in the OBL. Invoking Taylor's hypothesis, the residence time T of the largest (coherent) scales of motion λ in the ABL increases as $T \approx \lambda/U$ as they propagate over the OBL.

In the stable simulation *US*, the correlations are opposite to those in free convection (Fig. 12). The correlation between the near-surface atmospheric motions and the OBL motions is near zero, hence the small-scale structures in stably stratified turbulence propagate rapidly over the OBL. The spanwise spectra E_{vv} show a small ABL–OBL response at low wavenumbers in simulation *US* (not shown).

Figure 15 shows the spanwise spectra E_{vv} for a shear-convective regime dominated by rolls (upper panel) and a convective regime dominated by surface convective cells (lower panel). Just right of the spectral peak, the roll regime displays a spectral slope k_y^n with $n = -1.1$, while in the convective regime, a steeper spectral slope $n = -1.9$ is found. This striking contrast in the spectrum shapes between these two regimes and the slope values themselves are approximately confirmed in along-wind spectra from recent S-MODE observations (Wineteer et al. 2024).

5. Conclusions

The marine atmospheric boundary layer (ABL) and oceanic boundary layer (OBL) are a coupled dynamical system with two-way feedbacks depending on scale and oceanic surface heterogeneity (McWilliams 2016; Taylor and Thompson 2023). To investigate the interaction mechanisms, a coupled large-eddy simulation code is developed and exercised over a range of atmospheric stability $\infty > -h/L > 2.4$; h and L are the ABL depth and Monin–Obukhov stability parameter, respectively. In the simplest setup of a nominally horizontally

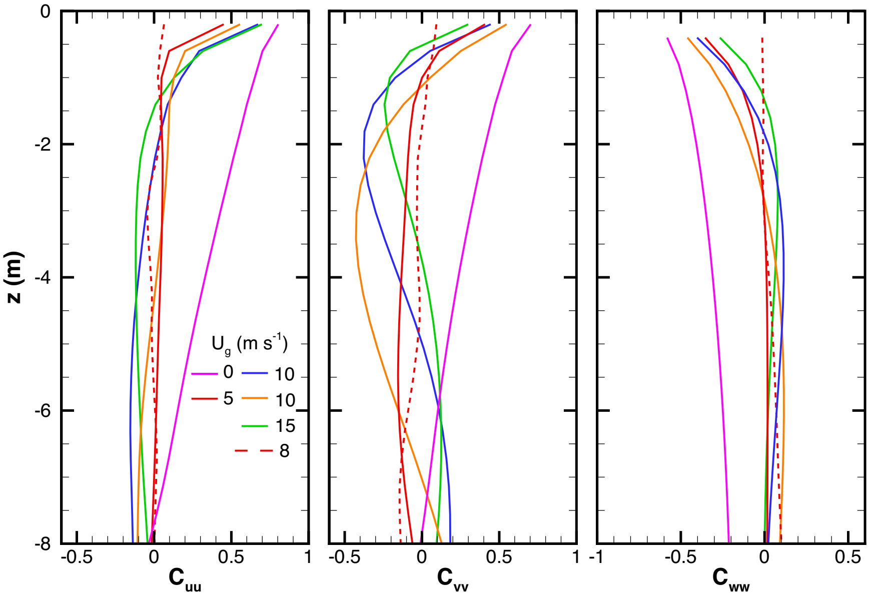

FIG. 12. Profiles of the correlation coefficients (C_{uu}, C_{vv}, C_{ww}) between the fluctuating $\mathbf{u}'$ velocity at the 10-m reference height in the atmosphere and the fluctuating ocean $\mathbf{u}'$ velocity. The colored lines (pink, red, blue, orange, green) are simulations (*UF*, *U*5, *U*10, *U*10*C*, *U*15). The correlation coefficients (left) C_{uu}, (middle) C_{vv}, and (right) C_{ww}. Data in the atmosphere and ocean are filtered at $\delta = 500$ m using an isotropic filter. The stable simulation $U_g = 8$ m s^{-1}, *US*, shown by the long dash red line uses a filter with $\delta = 150$ m. The correlation coefficients are zero for simulations that utilize x–y average coupling (not shown).

homogeneous ABL and OBL, we find that the largest scale turbulent structures in the atmospheric boundary layer, i.e., the atmospheric plumes and turbulent shear-convective rolls (SCRs), leave an imprint on the oceanic boundary layer. This is shown by comparing simulations that use instantaneous point-by-point spatial coupling rules at the oceanic surface versus similarly configured simulations that use spatially x–y average coupling rules, i.e., the large-scale spatially

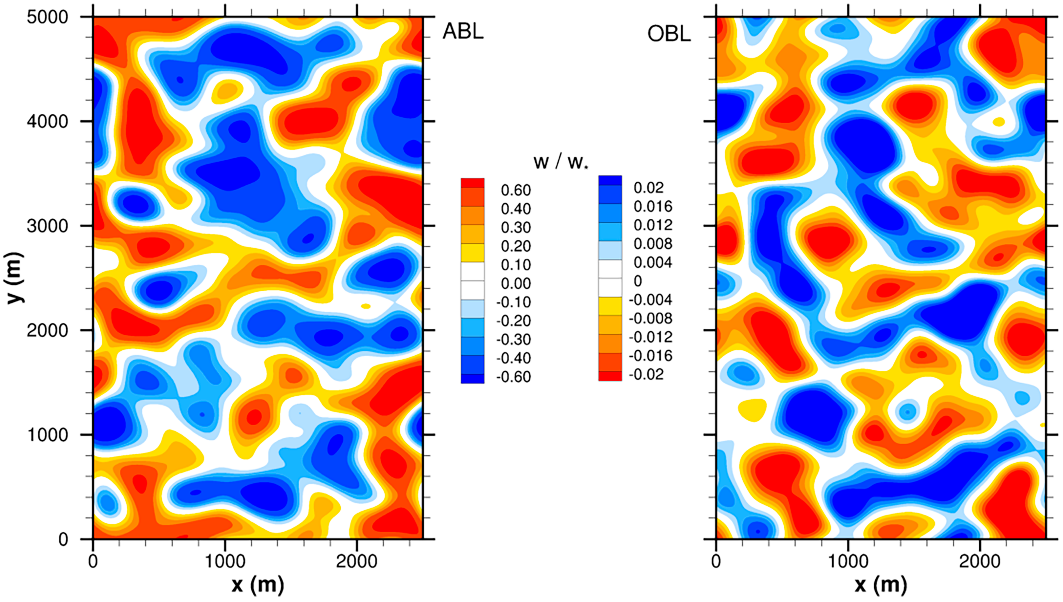

FIG. 13. Vertical velocity w/w_* in the (left) ABL at $z = 9.02$ m and (right) OBL at $z = -1.2$ m under free convection (simulation *UF*). The same isotropic filter $\delta = 500$ m is used in the ABL and OBL. The coherent structures in the atmosphere leave an imprint in the ocean leading to the negative correlation in Fig. 12. Note that the color bar in the ocean is reversed compared to its atmospheric counterpart.

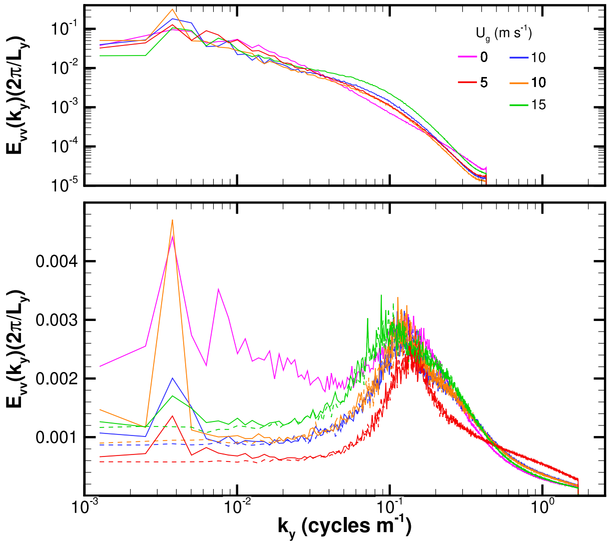

FIG. 14. Spectra of spanwise velocity E_{vv} for varying spanwise wavenumber k_y in the (top) atmosphere and (bottom) ocean under varying geostrophic winds. Simulations $U5$, $U10$, and $U15$ are indicated by red, blue, and green lines, respectively. The orange line is $U10C$ that imposes a larger initial temperature jump $\delta\theta_i = 3$ K. Free convection UF is indicated by a pink line. In the bottom panel, the dashed lines are identical simulations, but with x–y average coupling conditions. Spectra are normalized by the appropriate (ABL, OBL) friction velocity u_*^2, and in the simulation UF by w_*^2. The shear-convective turbulence in the ABL leaves an imprint on the OBL at low wavenumbers $k_y \sim 0.004$ m^{-1} or wavelength ratios $\lambda/h > 70$.

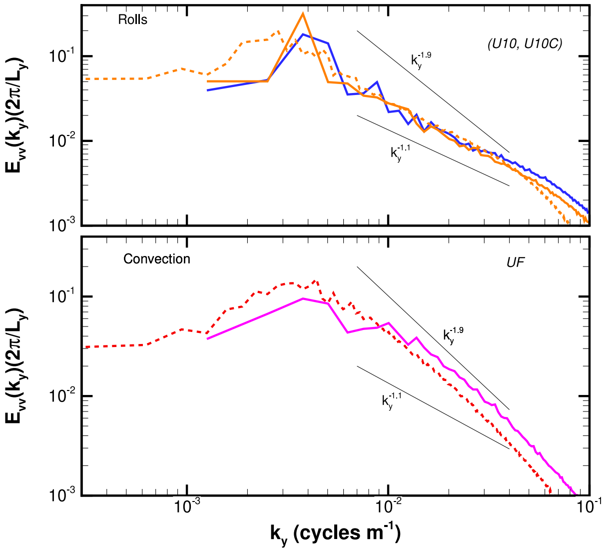

FIG. 15. Atmospheric spanwise spectra of spanwise velocity E_{vv} for varying spanwise wavenumber k_y in the shear-convective regime dominated by (top) SCR and (bottom) convective cells. Simulations $U10$ and $U10C$ are denoted by blue and orange lines, respectively, are shown in the top panel. The free convection simulation UF denoted by a pink line is shown in the bottom panel. The dotted lines show the results from uncoupled ABL simulations in a larger horizontal domain, (20, 20) km domain with horizontal grid mesh (2048, 2048). The dotted orange line in the top panel is $U_g = 10$ m s, $Q_{v,*} = 0.024\,\mathrm{K\,m\,s^{-1}}$, and $-h/L = 7.1$. The dotted red line in the bottom panel is $U_g = 1.0$ m s^{-1}, $Q_{v,*} = 0.01\,\mathrm{K\,m\,s^{-1}}$, and $-h/L > 830$. The thin black lines are spectral slopes k_y^n where $n = (-1.1, -1.9)$.

intermittent turbulent structures in the atmosphere modulate the sea surface temperature (SST), currents, and the connecting momentum and temperature fluxes. The impact on the total (resolved plus SGS) spanwise momentum flux $\langle -v'w' \rangle$ in the ABL, i.e., the momentum flux component perpendicular to the mean wind direction, is small but persistent with the largest effect for a geostrophic wind speed $U_g = 10$ m s^{-1}.

In the OBL, the SCRs leave an imprint on the currents at low wavenumbers over a stability dependent depth of approximately 5 m. Spectra of the spanwise current $E_{vv}(k_y)$ show a clear secondary spectral peak at wavenumbers $2\pi/(hk_y) = \lambda/h \sim 70$ or more. Spatially filtering the ABL winds and OBL currents at a scale $\delta = 500$ m shows correlations between the ABL winds at the 10-m reference height and the oceanic currents; the horizontal correlations vary from 1 at the surface to -0.5 at $z \sim -4$ m for simulations that use point-by-point coupling conditions; similarly configured simulations that utilize x–y average coupling have zero correlation between the ABL winds and the oceanic currents. A negative correlation is found between vertical velocity w in the ABL and OBL. (Updrafts, downdrafts) in the ABL are anticorrelated with (downdrafts, updrafts) in the OBL to impose the no-flow surface boundary condition. Under free convective conditions, where the ABL near-surface hexagonal pattern slowly evolves, the signature of the large-scale convective plumes is readily visible in the OBL. An indirect effect of our LES coupling shows that Langmuir turbulence enhances the OBL entrainment flux compared to the ABL entrainment. Thus, while the ABL in the shear-convective regime scales with the Deardorff velocity scale w_*, the OBL scales with the surface friction velocity u_* with interior mixing are also dependent on the wave field.

While many of the statistical properties in the OBL and ABL are only modestly changed by air–sea coupling in the locally homogeneous cases examined here, we might expect larger changes when the interface is heterogeneous due to oceanic submesoscale fronts and eddies; this is a topic for future research.

Acknowledgments. PPS and JCM were supported by the Office of Naval Research through the Physical Oceanography Program (Awards N00014-17-1-2334, N00014-23-1-2053, and N00014-18-1-2599) and by the National Oceanic and Atmospheric Administration Award NA19OAR4310378. PPS and EGP acknowledge the support from the National Science Foundation (Award 2103874) with the Johns Hopkins University to the National Center for Atmospheric Research (NCAR) (Subaward 2005117865) and the Geophysical Turbulence Program at NCAR. This research benefited greatly from computer resources provided by the Department of Defense High Performance Computing Modernization Program and NCAR's Computational and Information Systems

Laboratory (https://doi.org/10.5065/D6RX99HX) sponsored by the National Science Foundation. We thank two reviewers who provided comments that improved the manuscript. We also thank the S-MODE team for providing us early access to their observational data.

Data availability statement. The simulation profiles and visualization data are available from the authors on request.

REFERENCES

Alcayaga, L., G. C. Larsen, M. Kelly, and J. Mann, 2022: Large-scale coherent turbulence structures in the atmospheric boundary layer over flat terrain. *J. Atmos. Sci.*, **79**, 3219–3243, https://doi.org/10.1175/JAS-D-21-0083.1.

Belcher, S. E., and Coauthors, 2012: A global perspective on Langmuir turbulence in the ocean surface boundary layer. *Geophys. Res. Lett.*, **39**, L18605, https://doi.org/10.1029/2012GL052932.

Bendat, J. S., and A. G. Piersol, 1971: *Random Data: Analysis and Measurement Procedures*. John Wiley and Sons, 407 pp.

Brilouet, P.-E., J.-L. Redelsperger, M.-N. Bouin, F. Couvreux, and C. L. Brossier, 2021: A case-study of the coupled ocean–atmosphere response to an oceanic diurnal warm layer. *Quart. J. Roy. Meteor. Soc.*, **147**, 2008–2032, https://doi.org/10.1002/qj.4007.

——, ——, ——, ——, and N. Villefranque, 2024: A numerical study of ocean surface-layer response to atmospheric shallow convection: Impact of cloud shading, rain, and cold pools. *Quart. J. Roy. Meteor. Soc.*, **150**, 1401–1419, https://doi.org/10.1002/qj.4651.

Chen, W., M. L. Banner, E. J. Walsh, J. B. Jensen, and S. Lee, 2001: The Southern Ocean Waves Experiment. Part II: Sea surface response to wind speed and wind stress variations. *J. Phys. Oceanogr.*, **31**, 174–198, https://doi.org/10.1175/1520-0485(2001)031<0174:TSOWEP>2.0.CO;2.

Conzemius, R. J., and E. Fedorovich, 2006: Dynamics of sheared convective boundary layer entrainment. Part I: Methodological background and large-eddy simulations. *J. Atmos. Sci.*, **63**, 1151–1178, https://doi.org/10.1175/JAS3691.1.

Cronin, M. F., and Coauthors, 2019: Air-sea fluxes with a focus on heat and momentum. *Front. Mar. Sci.*, **6**, 430, https://doi.org/10.3389/fmars.2019.00430.

D'Asaro, E. A., J. Thomson, A. Y. Shcherbina, R. R. Harcourt, M. F. Cronin, M. A. Hemer, and B. Fox-Kemper, 2014: Quantifying upper ocean turbulence driven by surface waves. *Geophys. Res. Lett.*, **41**, 102–107, https://doi.org/10.1002/2013GL058193.

Deardorff, J. W., 1970: Convective velocity and temperature scales for the unstable planetary boundary layer and for Rayleigh convection. *J. Atmos. Sci.*, **27**, 1211–1213, https://doi.org/10.1175/1520-0469(1970)027<1211:CVATSF>2.0.CO;2.

——, 1972: Numerical investigation of neutral and unstable planetary boundary layers. *J. Atmos. Sci.*, **29**, 91–115, https://doi.org/10.1175/1520-0469(1972)029<0091:NIONAU>2.0.CO;2.

——, 1980: Stratocumulus-capped mixed layers derived from a three-dimensional model. *Bound.-Layer Meteor.*, **18**, 495–527, https://doi.org/10.1007/BF00119502.

Edson, J., and Coauthors, 2007: The coupled boundary layers and air–sea transfer experiment in low winds. *Bull. Amer. Meteor. Soc.*, **88**, 341–356, https://doi.org/10.1175/BAMS-88-3-341.

Fairall, C. W., E. F. Bradley, J. S. Godfrey, G. A. Wick, J. B. Edson, and G. S. Young, 1996: Cool-skin and warm-layer effects on sea surface temperature. *J. Geophys. Res.*, **101**, 1295–1308, https://doi.org/10.1029/95JC03190.

——, ——, J. E. Hare, A. A. Grachev, and J. B. Edson, 2003: Bulk parameterization of air–sea fluxes: Updates and verification for the COARE algorithm. *J. Climate*, **16**, 571–591, https://doi.org/10.1175/1520-0442(2003)016<0571:BPOASF>2.0.CO;2.

Farrar, J. T., and Coauthors, 2020: S-MODE: The sub-mesoscale ocean dynamics experiment. *IGARSS 2020-2020 IEEE Int. Geoscience and Remote Sensing Symp.*, Waikoloa, HI, Institute of Electrical and Electronics Engineers, 3533–3536, https://doi.org/10.1109/IGARSS39084.2020.9323112.

Fulgosi, M., D. Lakehal, S. Banerjee, and V. De Angelis, 2003: Direct numerical simulation of turbulence in a sheared air–water flow with a deformable interface. *J. Fluid Mech.*, **482**, 319–345, https://doi.org/10.1017/S0022112003004154.

Gula, J., M. J. Molemaker, and J. C. McWilliams, 2014: Submesoscale cold filaments in the Gulf Stream. *J. Phys. Oceanogr.*, **44**, 2617–2643, https://doi.org/10.1175/JPO-D-14-0029.1.

Hamlington, P. E., L. P. Van Roekel, B. Fox-Kemper, K. Julien, and G. P. Chini, 2014: Langmuir–submesoscale interactions: Descriptive analysis of multiscale frontal spindown simulations. *J. Phys. Oceanogr.*, **44**, 2249–2272, https://doi.org/10.1175/JPO-D-13-0139.1.

Hanley, K. E., S. E. Belcher, and P. P. Sullivan, 2010: A global climatology of wind–wave interaction. *J. Phys. Oceanogr.*, **40**, 1263–1282, https://doi.org/10.1175/2010JPO4377.1.

Harcourt, R. R., and E. A. D'Asaro, 2008: Large-eddy simulation of Langmuir turbulence in pure wind seas. *J. Phys. Oceanogr.*, **38**, 1542–1562, https://doi.org/10.1175/2007JPO3842.1.

Harris, J. A., S. E. Belcher, and R. L. Street, 1996: Linear dynamics of wind waves in coupled turbulent air–water flow. Part 2. Numerical model. *J. Fluid Mech.*, **308**, 219–254, https://doi.org/10.1017/S0022112096001462.

Heus, T., and Coauthors, 2010: Formulation of the Dutch Atmospheric Large-Eddy Simulation (DALES) and overview of its applications. *Geosci. Model Dev.*, **3**, 415–444, https://doi.org/10.5194/gmd-3-415-2010.

Jayaraman, B., and J. G. Brasseur, 2021: Transition in atmospheric boundary layer turbulence structure from neutral to convective, and large-scale rolls. *J. Fluid Mech.*, **913**, A42, https://doi.org/10.1017/jfm.2021.3.

Kristovich, D. A. R., 1993: Mean circulations of boundary-layer rolls in lake-effect snow storms. *Bound.-Layer Meteor.*, **63**, 293–315, https://doi.org/10.1007/BF00710463.

Kukulka, T., A. J. Plueddemann, J. H. Trowbridge, and P. P. Sullivan, 2010: Rapid mixed layer deepening by the combination of Langmuir and shear instabilities: A case study. *J. Phys. Oceanogr.*, **40**, 2381–2400, https://doi.org/10.1175/2010JPO4403.1.

——, ——, and P. P. Sullivan, 2013: Inhibited upper ocean restratification in nonequilibrium swell conditions. *Geophys. Res. Lett.*, **40**, 3672–3676, https://doi.org/10.1002/grl.50708.

Large, W. G., and S. Pond, 1981: Open ocean momentum flux measurements in moderate to strong winds. *J. Phys. Oceanogr.*, **11**, 324–336, https://doi.org/10.1175/1520-0485(1981)011<0324:OOMFMI>2.0.CO;2.

Leibovich, S., 1983: The form and dynamics of Langmuir circulations. *Annu. Rev. Fluid Mech.*, **15**, 391–427, https://doi.org/10.1146/annurev.fl.15.010183.002135.

LeMone, M. A., 1973: The structure and dynamics of horizontal roll vortices in the planetary boundary layer. *J. Atmos. Sci.*,

30, 1077–1091, https://doi.org/10.1175/1520-0469(1973)030<1077:TSADOH>2.0.CO;2.

Mahadevan, A., A. Pascual, D. L. Rudnick, S. Ruiz, J. Tintoré, and E. D'Asaro, 2021: CALYPSO: Observing coherent pathways from the surface ocean to the interior. *Bull. Amer. Meteor. Soc.*, **102**, 532–540, https://doi.org/10.1175/BAMS-D-19-0305.A.

Mazella, E., T. Hara, and P. P. Sullivan, 2024: Reduction of drag coefficient due to misaligned wind-waves. *J. Geophys. Res. Oceans*, **129**, e2023JC020593, https://doi.org/10.1029/2023JC020593.

McWilliams, J. C., 2016: Submesoscale currents in the ocean. *Proc. Roy. Soc. London*, **472A**, 20160117, https://doi.org/10.1098/rspa.2016.0117.

——, 2021: Oceanic frontogenesis. *Annu. Rev. Mar. Sci.*, **13**, 227–253, https://doi.org/10.1146/annurev-marine-032320-120725.

——, 2022: *Quasi-Linear Theory for Surface Wave-Current Interactions*. Springer, 125 pp., https://doi.org/10.1007/978-981-19-2876-5.

——, P. P. Sullivan, and C.-H. Moeng, 1997: Langmuir turbulence in the ocean. *J. Fluid Mech.*, **334**, 1–30, https://doi.org/10.1017/S0022112096004375.

Moeng, C.-H., 1984: A large-eddy-simulation model for the study of planetary boundary-layer turbulence. *J. Atmos. Sci.*, **41**, 2052–2062, https://doi.org/10.1175/1520-0469(1984)041<2052:ALESMF>2.0.CO;2.

——, and P. P. Sullivan, 1994: A comparison of shear- and buoyancy-driven planetary boundary layer flows. *J. Atmos. Sci.*, **51**, 999–1022, https://doi.org/10.1175/1520-0469(1994)051<0999:ACOSAB>2.0.CO;2.

——, and ——, 2015: Large-eddy simulation. *Encyclopedia of Atmospheric Sciences*, 2nd ed. G. R. North, F. Zhang, and J. Pyle, Eds., Vol. 4, Academic Press, 232–240, https://doi.org/10.1017/CBO9780511184053.

Moum, J. N., and Coauthors, 2014: Air–sea interactions from westerly wind bursts during the November 2011 MJO in the Indian Ocean. *Bull. Amer. Meteor. Soc.*, **95**, 1185–1199, https://doi.org/10.1175/BAMS-D-12-00225.1.

Munk, W., L. Armi, K. Fischer, and F. Zachariasen, 2000: Spirals on the sea. *Proc. Roy. Soc.*, **456A**, 1217–1280, https://doi.org/10.1098/rspa.2000.0560.

Nurser, A. J. G., and S. M. Griffies, 2019: Relating the diffusive salt flux just below the ocean surface to boundary freshwater and salt fluxes. *J. Phys. Oceanogr.*, **49**, 2365–2376, https://doi.org/10.1175/JPO-D-19-0037.1.

Perlin, N., S. P. de Szoke, D. B. Chelton, R. M. Samelson, E. D. Skyllingstad, and L. W. O'Neill, 2014: Modeling the atmospheric boundary layer wind response to mesoscale sea surface temperature perturbations. *Mon. Wea. Rev.*, **142**, 4284–4307, https://doi.org/10.1175/MWR-D-13-00332.1.

Pope, S. B., 2000: *Turbulent Flows*. Cambridge University Press, 771 pp., https://doi.org/10.1016/B978-0-12-382225-3.00201-2.

Renault, L., P. Marchesiello, S. Masson, and J. C. McWilliams, 2019: Remarkable control of western boundary currents by *eddy killing*, a mechanical air-sea coupling process. *Geophys. Res. Lett.*, **46**, 2743–2751, https://doi.org/10.1029/2018GL081211.

Richter, D. H., A. E. Dempsey, and P. P. Sullivan, 2019: Turbulent transport of spray droplets in the vicinity of moving surface waves. *J. Phys. Oceanogr.*, **49**, 1789–1807, https://doi.org/10.1175/JPO-D-19-0003.1.

Salesky, S. T., M. Chamecki, and E. Bou-Zeid, 2017: On the nature of the transition between roll and cellular organization in the convective boundary layer. *Bound.-Layer Meteor.*, **163**, 41–68, https://doi.org/10.1007/s10546-016-0220-3.

Schmidt, H., and U. Schumann, 1989: Coherent structure of the convective boundary layer derived from large-eddy simulations. *J. Fluid Mech.*, **200**, 511–562, https://doi.org/10.1017/S0022112089000753.

Shen, L., and D. K. P. Yue, 2001: Large-eddy simulation of free-surface turbulence. *J. Fluid Mech.*, **440**, 75–116, https://doi.org/10.1017/S0022112001004669.

Shroyer, E., and Coauthors, 2021: Bay of Bengal intraseasonal oscillations and the 2018 monsoon onset. *Bull. Amer. Meteor. Soc.*, **102**, E1936–E1951, https://doi.org/10.1175/BAMS-D-20-0113.1.

Stull, R. B., 1988: *An Introduction to Boundary Layer Meteorology*. Kluwer Academic Publishers, 666 pp., https://doi.org/10.1007/978-94-009-3027-8.

Sullivan, P. P., and J. C. McWilliams, 2010: Dynamics of winds and currents coupled to surface waves. *Annu. Rev. Fluid Mech.*, **42**, 19–42, https://doi.org/10.1146/annurev-fluid-121108-145541.

——, and E. G. Patton, 2011: The effect of mesh resolution on convective boundary layer statistics and structures generated by large-eddy simulation. *J. Atmos. Sci.*, **68**, 2395–2415, https://doi.org/10.1175/JAS-D-10-05010.1.

——, and J. C. McWilliams, 2018: Frontogenesis and frontal arrest of a dense filament in the oceanic surface boundary layer. *J. Fluid Mech.*, **837**, 341–380, https://doi.org/10.1017/jfm.2017.833.

——, and ——, 2019: Langmuir turbulence and filament frontogenesis in the oceanic surface boundary layer. *J. Fluid Mech.*, **879**, 512–553, https://doi.org/10.1017/jfm.2019.655.

——, and ——, 2022: Atmospheric boundary layers over an oceanic eddy. *J. Atmos. Sci.*, **79**, 2601–2620, https://doi.org/10.1175/JAS-D-22-0019.1.

——, and ——, 2024: Oceanic frontal turbulence. *J. Phys. Oceanogr.*, **54**, 333–358, https://doi.org/10.1175/JPO-D-23-0033.1.

——, ——, and W. K. Melville, 2007: Surface gravity wave effects in the oceanic boundary layer: Large-eddy simulation with vortex force and stochastic breakers. *J. Fluid Mech.*, **593**, 405–452, https://doi.org/10.1017/S002211200700897X.

——, L. Romero, J. C. McWilliams, and W. K. Melville, 2012: Transient evolution of Langmuir turbulence in ocean boundary layers driven by hurricane winds and waves. *J. Phys. Oceanogr.*, **42**, 1959–1980, https://doi.org/10.1175/JPO-D-12-025.1.

——, J. C. McWilliams, and E. G. Patton, 2014: Large-eddy simulation of marine atmospheric boundary layers above a spectrum of moving waves. *J. Atmos. Sci.*, **71**, 4001–4027, https://doi.org/10.1175/JAS-D-14-0095.1.

——, J. C. Weil, E. G. Patton, H. J. J. Jonker, and D. V. Mironov, 2016: Turbulent winds and temperature fronts in large-eddy simulations of the stable atmospheric boundary layer. *J. Atmos. Sci.*, **73**, 1815–1840, https://doi.org/10.1175/JAS-D-15-0339.1.

——, J. C. McWilliams, J. C. Weil, E. G. Patton, and H. J. S. Fernando, 2020: Marine boundary layers above heterogeneous SST: Across-front winds. *J. Atmos. Sci.*, **77**, 4251–4275, https://doi.org/10.1175/JAS-D-20-0062.1.

——, ——, ——, ——, and ——, 2021: Marine boundary layers above heterogeneous SST: Alongfront winds. *J. Atmos. Sci.*, **78**, 3297–3315, https://doi.org/10.1175/JAS-D-21-0072.1.

Suzuki, N., and B. Fox-Kemper, 2016: Understanding Stokes forces in the wave-averaged equations. *J. Geophys. Res. Oceans*, **121**, 3579–3596, https://doi.org/10.1002/2015JC011566.

Sykes, R. I., and D. S. Henn, 1989: Large-eddy simulation of turbulent sheared convection. *J. Atmos. Sci.*, **46**, 1106–1118, https://doi.org/10.1175/1520-0469(1989)046<1106:LESOTS>2.0.CO;2.

Taylor, J. R., and A. F. Thompson, 2023: Submesoscale dynamics in the upper ocean. *Annu. Rev. Fluid Mech.*, **55**, 103–127, https://doi.org/10.1146/annurev-fluid-031422-095147.

Weckwerth, T. M., J. W. Wilson, R. M. Wakimoto, and N. A. Crook, 1997: Horizontal convective rolls: Determining the environmental conditions supporting their existence and characteristics. *Mon. Wea. Rev.*, **125**, 505–526, https://doi.org/10.1175/1520-0493(1997)125<0505:HCRDTE>2.0.CO;2.

Wineteer, A., E. Rodriguez, D. Perkovic Martin, H. Torres, F. Polverari, R. Akbar, and C. Rocha, 2024: Exploring the characteristics of ocean surface winds at high resolution with Doppler scatterometry. *Geophys. Res. Lett.*, **51**, e2024GL113455, https://doi.org/10.1029/2024GL113455.

Wong, E. W., and P. J. Minnett, 2018: The response of the ocean thermal skin layer to variations in incident infrared radiation. *J. Geophys. Res. Oceans*, **123**, 2475–2493, https://doi.org/10.1002/2017JC013351.

Wyngaard, J. C., 2010: *Turbulence in the Atmosphere*. Cambridge University Press, 393 pp., https://doi.org/10.1017/CBO9780511840524.

——, L. J. Peltier, and S. Khanna, 1998: LES in the surface layer: Surface fluxes, scaling, and SGS modeling. *J. Atmos. Sci.*, **55**, 1733–1754, https://doi.org/10.1175/1520-0469(1998)055<1733:LITSLS>2.0.CO;2.